ETSI-Compliant Protection of Connected Vulnerable Road Users: Simulation and Field Trial

International Journal of Mechanical Sciences 284 (2024) 109731

Contents lists available at ScienceDirect

International Journal of Mechanical Sciences

journal homepage: www.elsevier.com/locate/ijmecsci

Mechanical interactions modeling of inertial wave energy converters

Fabio Carapellese *, Nicolás Faedo

Marine Offshore Renewable Energy Lab., Department of Mechanical and Aerospace Engineering, Politecnico di Torino, 10129 Turin, Italy

ARTICLE INFO

Keywords:
Nonlinear simulation
Inertial reaction mass wave energy converter
Lagrange equation
Pendulum dynamic equation
Bearing loads

ABSTRACT

Numerous technological solutions for wave energy converters (WECs), referred as inertial reaction mass (IRM) systems, incorporate a reacting mass within the floater, coupled with a power take-off (PTO) system, to shelter all electronic components from the hostile sea environment. While the overall complexity of the system increases, the current modeling procedures persist in considering only a limited number of modes of motion, neglecting relevant dynamical effects. In this context, this paper proposes a systematic procedure for defining the kinematic characteristics and overall analytical model for the dynamics of IRM WECs. The significance of the proposed procedure lies in the statement of the reaction mass-related dynamic equation, considering the floater's parametric excitation in six degrees of freedom (DoF). Additionally, it introduces the procedure for defining the reaction forces that the inertial mass exerts on the floater, which are often neglected in the literature for the full simulation of such systems. Furthermore, the proposed analytical modeling procedure allows the definition of approximated models in more simplified nonlinear forms for dynamic analysis and ultimately in fully linear approximations. This enables the application of methodologies and techniques commonly used in the literature for linear systems. The development of the framework is kept generic, in order to introduce a versatile mathematical procedure, that can be easily adjusted, with minor modifications, to accurately capture and represent the mechanical interaction for a wide family of IRM WEC devices. Subsequently, a case study on a vertical-hinged pendulum WEC is analyzed, to showcase the effectiveness of the proposed methodology. Moreover, to test the reliability of the analytical framework, a comparison with the output of a commercial software is conducted.

1. Introduction

In 2019 alone, humans released 36.7 billion tons of CO_2, marking a staggering 50% increase compared to the year 2000, causing consequent increment of heat trapped in the atmosphere. This includes the use of gas-powered vehicles, livestock farming, intensive agriculture, deforestation, waste generation, and the combustion of coal, oil, and natural gas for electricity and heat production [1]. The latter contributes a quarter of global human-driven emissions. It is then absolutely clear that any efforts in mitigating climate change necessitate a reduction in greenhouse gas emissions on a global scale. As the energy sector plays a pivotal role, the International Renewable Energy Agency (IRENA) indicates the path, technologically speaking, for decarbonizing the power sector, which relies on the vast expansion of renewable electricity generation and on the expansion of smarter and more flexible electricity grid. In most parts of the world today, renewable energies have become the lowest cost source of power generation, and are generally competitive when directly compared with fossil alternatives. In this context, wave energy emerges is a promising renewable energy source, potentially fulfilling up to one third of the global energy demand [2,3]. Although wave power has several advantages, *e.g.* high level of power intensity source availability over time, wave energy conversion technologies have not yet reached commercialization stage, when compared to well-established renewable energy sources, *e.g* wind and solar. It is worth highlighting that numerous concepts and prototypes of WEC systems have been developed and built by inventors and researchers in recent decades [4,5], with the final aim of exploiting the reciprocating motion of the sea wave to produce clean energy.

Since the early beginning, it has been clear that converting wave energy into usable power is not straightforward, mostly since mechanical and electrical components are challenged by the harsh sea environment, where the level of corrosion and wear have an enormous impact on the overall system durability and functionality. Therefore, to overcome these difficulties, it is common to install energy conversion systems within a sealed hull, sheltering all main electronic/mechanical components from the marine environment. These systems are referred to as Inertial Reaction Mass (IRM) WECs. Although useful to reduce the harsh effects from the sea, this development adds further complexity to

* Corresponding author.
E-mail addresses: fabio.carapellese@polito.it (F. Carapellese), nicolas.faedo@polito.it (N. Faedo).

https://doi.org/10.1016/j.ijmecsci.2024.109731
Received 30 April 2024; Received in revised form 11 September 2024; Accepted 12 September 2024
Available online 24 September 2024

Nomenclature

α	Generalized coordinate about ξ-axis
β	Generalized coordinate about η-axis
γ	Generalized coordinate about ζ-axis
B_F	Floater Coriolis matrix in $\mathcal{R}(\mathcal{O}'\text{xyz})$
B_f	Floater Coriolis matrix in $\mathcal{R}(\mathcal{O}\text{XYZ})$
B_I	Mechanism Coriolis matrix in $\mathcal{R}(\mathcal{G}\xi\eta\zeta)$
B_i	Total Coriolis matrix in $\mathcal{R}(\mathcal{O}\text{XYZ})$
C	3-D Rotation matrix
C_1	PTO output force
C_2	Generator control force
C_m	Hull-generated parametric excitation
c_{pto}	Control damping coefficient
D	Analytical Jacobian
$\mathcal{D}_u$	Mechanism-related Jacobian matrix
$\mathcal{R}_u$	Mechanism-related rotation matrix
Φ	3-Dimensional rotation vector
F_{ext}	External hull force in the floater frame
f_{ext}	External hull force in the inertial frame
F_{rc}	Reaction forces in $\mathcal{R}(\mathcal{G}\xi\eta\zeta)$
f_{rc}	Reaction forces in $\mathcal{R}(\mathcal{O}'\text{xyz})$
$\bar{f}_{rc}$	Full mechanical coupling vector
f_{bk}	Damping and stiffness force vector
f_e	Wave excitation force
f_h	Hydrostatic force
f_r	Radiation force
I_m	Mechanism inertia matrix
I_{mf}	Inertial coupling vector
l_p	Pendulum arm
$\mathcal{M}$	Floater total mass matrix
M_F	Floater mass matrix in $\mathcal{R}(\mathcal{O}'\text{xyz})$
M_f	Floater Coriolis matrix in $\mathcal{R}(\mathcal{O}\text{XYZ})$
M_I	Mechanism mass matrix in $\mathcal{R}(\mathcal{G}\xi\eta\zeta)$
M_i	Total Coriolis matrix in $\mathcal{R}(\mathcal{O}\text{XYZ})$
$\bar{M}_F$	Linear mass matrix
m^∞	Added mass at the infinite frequency
m_p	Pendulum mass
J_F	Jacobian matrix to $\mathcal{R}(\mathcal{O}'\text{xyz})$
J_M	Jacobian matrix to $\mathcal{R}(\xi\eta\zeta)$
J_I	Jacobin matrix in $\mathcal{R}(\mathcal{G}\xi\eta\zeta)$
k_r	Radiation kernel
$\bar{K}$	Linear stiffness matrix
p	Mechanism pose vector
q	Floater pose vector
P_a	Instantaneous mechanical power
r	Mechanism position vector
ρ	Mechanism generalized coordinate
Σ	PTO representative function
s_h	Hydrostatic stiffness matrix
$\mathcal{T}$	Kinetic energy
$\mathcal{U}$	Potential energy
V_F	Floater linear velocity vector
V_I	Linear velocity vector in $\mathcal{R}(\mathcal{G}\xi\eta\zeta)$
V_g	Generator-related reaction force
V_r	PTO-related reaction force
V_{tot}	Reaction force on the mechanism DoF
V_M	Linear velocity vector in $\mathcal{R}(\mathcal{G}\Xi\mathcal{H}\mathcal{Z})$
V_{EF}	End-effector linear velocity vector
ω_m	Proper mechanism velocity vector
δ	Pitch rotation angle
θ	Roll rotation angle
ψ	Yaw rotation angle
Ω_F	Floater angular velocity vector
Ω_M	Angular velocity vector in $\mathcal{R}(\mathcal{G}\Xi\mathcal{H}\mathcal{Z})$
Ω_I	Angular velocity vector in $\mathcal{R}(\mathcal{G}\xi\eta\zeta)$
Ω_{EF}	End-effector linear velocity vector
$w_{\Xi\mathcal{H}\mathcal{Z}}$	Velocity vector in the $\mathcal{R}(\mathcal{G}\Xi\mathcal{H}\mathcal{Z})$
w_{xyz}	Velocity vector in $\mathcal{R}(\mathcal{O}'\text{xyz})$

the study of the underlying physical phenomena, since another stage in the energy conversion chain is included.

While the physical system indeed encompasses modeling of numerous energy transformation stages, addressing fluid–structure interaction and mechanical couplings represents the first challenge to provide a glimpse into the WEC potential. The hydrodynamic problem has been commonly faced, in the wave energy community, through the linear representation of the fluid effects on the floater, exploiting the so-called Cummins formulation [6,7]. Instead, mechanical interactions are commonly simulated through existing software, such as MATLAB® Simscape (commercial) or WEC-Sim (Wave Energy Converter SIMulator — non-commercial). The latter represents a suitable option, being an open-source code properly developed for WEC system simulation by the National Renewable Energy Laboratory and Sandia National Laboratories [8]. WEC-Sim uses a very intuitive approach through a connection of blocks for the description of the dynamic interactions between rigid bodies. However, an analytical expression is crucial for performing analysis on the system response and for the synthesis of model-based control strategies, for energy maximization purposes [9,10]. In most cases, when an analytical representation is derived within the literature, several simplifying assumptions are often made, by *e.g.* reducing the number of modeled degrees-of-freedom (DoF) to either one or three.

Note that, with reference to Fig. 1, we can classify the IRM WECs existing in the literature according to the architecture of the reacting system. In particular, IRM WEC devices rely on the coupling between two rigid bodies: the floater generates a parametric excitation to an encapsulated body which, behaving as a prime mover, activates the internal energy conversion mechanism for electric power production. The nature of the coupling can vary depending on the selected system design.

The literature review highlights various wave energy conversion mechanisms, that will be referred as Inertial Reaction Mass (IRM), including: (a) pendulum mechanism, (b) gyroscopic system, and (c) sliding mass. These architectures are classified based on the arrangements of the rotational axis, and on the coupling modes of the IRM with the WEC hull. The pendulum technology, for instance, can be adopted in WEC systems with its rotation axis being adjusted on a horizontal or vertical plane, according to the expected system interaction with the input wave [11]. As a matter of fact, horizontally-hinged pendulums are constrained to move on a vertical plane and are coupled with the floater via the pitch DoF while. The former solutions are usually mounted into prismatic floaters, hence these are commonly modeled considering exclusively one rotation DoF (pitch) and two linear displacements, happening in a plane perpendicular to the pendulum rotation axis.

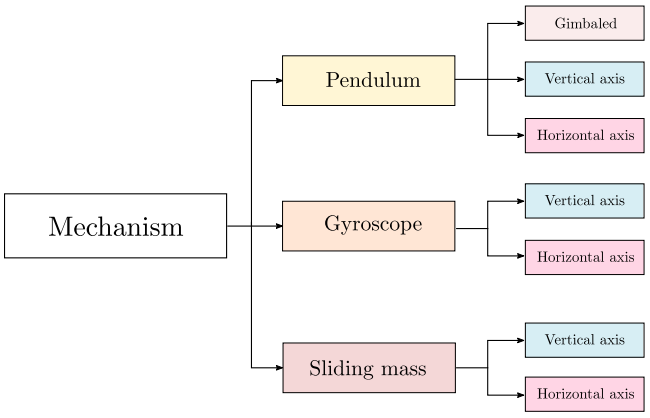

Fig. 1. Main mechanism applied to the energy transfer from wave to the electric generator.

The PeWEC system is an example of horizontal-axis pendulum WEC, whose floater pitching motion induces a swinging motion of the pendulum, being the energy extraction performed through the generator damping action on the harmonic motion of the pendulum [12]. Analysis on a pendulum-based IRM WEC is conducted also in [13]. Furthermore, the SEAREV [14] system exploits pendulum effects by connecting an eccentric mass, referenced to the hull, to an hydraulic PTO, which, in turn, sets an electric generator into motion [15–17]. Further example cases are the AMOG WEC [18], which is a pre-commercial scale device based on a horizontal pendulum architecture design, and the Seaquest [19], which incorporates a direct drive PTO, whose swing mass is itself the rotor of an electric generator. Although belonging to the horizontal-axis family of pendulum devices, the dynamic response of the system can change if the pendulum is mounted upside down. This system, called the inverted pendulum wave energy converter (IPWEC), is studied for WEC applications in [20].

Alternatively, vertical-axis pendulum are also considered being excited by vibrations generated from any direction, *i.e.* involving both roll and pitch rotations of the floater. For instance, in the study presented in [21], the use of nonlinear coupling between pitch and roll modes in a vessel is investigated, to increase power generation from the wave motion. For such a reason, this family of IRM WECs are mainly coupled with an axial-symmetric hull or irregular-shaped bodies, as in the case of the Penguin [22] and the VAPWEC [23]. To improve the system conversion capabilities for multi-directional inputs, the gimbaled-pendulum is a further technological solution that exploit the pendulum concept. Gimbaled pendulums for energy harvesting can be suspended by a thread, a universal joint, or multiple coupled shafts [24]. The WITT omnidirectional pendulum [25] is the most representative example of a gimbaled-type pendulum-based WEC, exhibiting a frequency response with three different peaks, whose broad banded operative frequency range impacts the system functionality [25].

Gyroscope-based systems, considering both inputs and outputs, involve three perpendicular rotation axes. Even though a 6-DoF model might be more suitable for such a family of systems, even in this case, for the sake of simplicity, some dynamics are commonly neglected, by constraining the system representation in a plane. Three prototypes of gyroscope-based systems have been designed and tested in the literature, as presented in [26]. In this setup, the electric generator can be activated by the gyroscopic rotation of a gimbal body referenced to a spinning flywheel [27]. The latter is the principle applied by both the ISWEC system [28], which controls the flywheel velocity to change the device frequency response, and the OCEANTEC device [29]. The gyroscope can alternatively be mounted with the vertical precession axis, as is the case of the GWEC [30].

The sliding body device, which involves the interaction between a floater and a sliding PTO system, is a further wave power absorption solutions proposed in the literature. The E-device [31] and the PS Frog Mk 5 [32] have successfully applied such as technological solution, allowing the mass t slide on the horizontal plane. For this family of devices, the mechanical motion is exploited to drive an electrical generator via a hydraulic transmission [32]. Alternatively, the reacting mass, encapsulated in the floater can be allowed to move on the vertical plane. The DR-WEC [33] and TALOS II belong to this class of devices. The latter system, presented in [34], is a multi-axis point absorber-style device with a solid outer hull encapsulating all moving parts. Another example is the vibro-impact WEC, as introduced in [35,36], which integrates a self-referenced mass mounted inside a semi-submerged floater to exploit the nonlinear elastic impact of the inner mass with the buoy, improving its power absorption capabilities.

In every category of IRM WECs under consideration, and across all existing technological solutions outlined in Table 1, modeling simplifications are virtually always adopted by the designers, to simplify the overall system description. These simplifications often involve neglecting certain dynamics or mechanical interactions, which are intentionally overlooked for practical reasons. Nonetheless, such assumptions can lead to misleading system representations, introducing a large degree of uncertainty in the main variables and indicators used to measure device performance, and hence actual estimation of the capabilities of any given IRM WEC. Furthermore, closed-form models are virtually always employed for control design purposes, which are fundamental for efficient and safe operation of WEC systems [37–39].

Motivated by the advantages of IRM WECs and the necessity for systematic and accurate modeling of this family of devices for performance assessment [40,41], optimization [42], and control purposes [43,44], this paper introduces a comprehensive yet simple methodology for modeling IRM WEC systems. This approach considers the full set of DoF and introduces a theoretical framework for their dynamic simulation, avoiding restrictive simplifications and incorporating all dynamic effects crucial for system design.

In particular, this paper provides the following main contributions:

- Derivation of the kinematic conversion chain, hence the analytical expressions describing the dynamic behavior of the reacting mass and its mechanical coupling with the floater, for a full set of DoF. This approach offers a comprehensive understanding of the interactions between rigid bodies in the wave energy conversion context.
- Definition of a generalized, step-by-step procedure for constructing kinematic transformation matrices, which can be applied to the Lagrange equation, defined for quasi-coordinates, to derive the equations of motion for a wide range of IRM WEC systems. This procedure ensures both broad applicability and ease of use.
- Loads computation on critical mechanical components, *e.g.* supporting bearings, addressing a crucial aspect of IRM WEC design and ensuring that the components are designed to meet the practical demands of their operational environment.

It is important highlighting the advantages of the analytical model presented. Specifically, it provides the WEC designer with a comprehensive understanding of the energy transformation process, including the overall occurring nonlinear effects. This model also facilitates the development of control-oriented models for designing and synthesizing control technologies. It can be achieved, through the creation of a simplified linear model for straightforward control algorithms with practical implementation value. For instance, a linear model derived from the nonlinear one is essential, especially for impedance-matching control methods [10,45]. Additionally, the introduction of the analytical equations allows simplifications that produce intermediate nonlinear models [37,39], for more effective analysis on the system response [46–48] and data-driven control algorithms [49], suited for nonlinear system representation. The remainder of this paper is organized as follows. Section 2 introduces the IRM WEC simulation loop,

Table 1
Classification of IRM WECs and model complexity. The marker color specify the motion axis of the related mechanism: light blue → horizontal axis, violet → vertical axis, and black → multiple axis. Moreover, the table acronyms are: Pr → Prismatic, Ax → Axial-symmetric, and Ir → irregular; While for the modeled DoFs: S → Surge, Sw → Sway, H → Heave, R → Roll, P → Pitch, Y → Yaw, M→ Mechanism-related DoF. Finally, Exp stands for performance analysis based on experimental activity.

Ref.	Name	Inertial mechanism			Floater shape	Modeled DoF
		Pendulum	Gyroscope	Sliding Mass		
[50,51]	ISWEC		■		Pr	S-H-P-M
[45,52]	PeWEC	■			Pr	S-H-P-M
[14,16]	SEAREV	■			Pr	S-H-P-M
[22]	Penguin	■			Ir	Exp
[25]	WITT	■			Ax	S-H-P-M
[31,53]	E-Motion			■	Pr	P-M
[30,54]	G-WEC		■		Pr	S-H-P-M
[32]	PS Frog MK 5			■	Ir	S-P-M
[35]	VIWEC			■	Ax	H-M
[29]	OCEANTEC		■		P	Exp
[20]	IPWEC	■			Pr	H-M
[18]	AMOG	■			Pr	Exp
[33]	DR-WEC			■	Ax	H-M
[23]	VAPWEC	■			Ax	S-Sw-H-R-P-M
[21]	WEC by Yerrapragada	■			A	R-P-M
[34]	TALOS II			■	Pr	Exp
[13]	WEC by Ma	■			Pr	P-M
[55]	Plumb Bob	■			Pr	Exp
[26]	WEC by Kanki		■		Pr	Exp
[19]	Seaquest	■			Pr	Exp

focusing on mathematical representation of the mechanical interactions. Section 3 addresses the kinematic problem of each interacting body, while Section 4 details the approach for formulating the complete set of dynamic equations. In Section 5, the modeling of a specific vertically-hinged pendulum IRM WEC is presented, while Section 6 introduces a comparison between the output of the analytical model with the one computed by the commercial software Simscape. Finally, Section 7 encompasses the main conclusions of this manuscript.

Notation

The notation $R(\alpha, \hat{k})$ represents a rotation by an angle α around the versor $\hat{k}$. The symbol 0 is used to denote a zero matrix, with dimensions that are understood based on the context. Furthermore, for a general vector $\chi = [\chi_x,\ \chi_y,\ \chi_z]^\mathsf{T}$, the corresponding skew-symmetric matrix is denoted by $\tilde{\chi}$. For a square matrix $B \in \mathbb{R}^{m\times m}$, we define $B^{-\mathsf{T}}$ as the transpose of the inverse of B, denoted by $(B^{-1})^\mathsf{T}$. Furthermore, $\bar{I}_n$ specify the identity matrix in $\mathbb{C}^{n\times n}$. Defined the matrix $M \in \mathbb{C}^{n\times m}$, we denote its ij-th entry as M_{ij}, with $i \in \mathbb{N}_n$ and $j \in \mathbb{N}_m$. Similarly, for a vector $V \in \mathbb{R}^n$, we refer to its ith component as V_i, where $i \in \mathbb{N}_n$. Additionally, we define the canonical basis vector as $e_i^j \in \mathbb{R}^j$, characterized by all components being zero except for the $i-$th element, which is 1.

2. On the integration of the mechanical model into the WEC simulation scheme

IRM WECs are generally identified as point absorbers [56], characterized by an inertial body, installed in a floater, moored to the seabed. The electrical and electronic components of these systems are enclosed into the hull to avoid issues with corrosion (as per the discussion provided in Section 1), enabling the mitigation of issues related to maintenance and accessibility of these hardware components. As shown in Fig. 2, this set of devices generally introduces a further step in the energy conversion process. For instance, the hydrodynamic interaction between the floater and the wave induces a parametric excitation to the inertial body installed in the hull. While the inertial system activates the PTO for electric power generation, the reaction forces are fed back to floater, impacting significantly its dynamics. Furthermore, the produced power can then be either stored, or directly supplied into the grid. Focusing on mechanical power characterization, we introduce the IRM WEC simulation framework. The fluid–structure interaction modeling is first generally introduced in Section 2.1. The physical characterization of the reaction forces is presented in Section 2.2, and the overall general model is presented in Section 2.3.

2.1. Modeling of the fluid–structure interaction

As mentioned in Section 1, the fluid–structure interaction mathematically represents the initial modeling challenge, when approaching the simulation of a WEC system. Although the problem can become significantly demanding [57–59], the use of a linear representation of hydrodynamic phenomena is well-established for the initial power assessment of such systems. Particularly, under the assumption of an irrotational flow and neglecting viscous effects, the *linear potential flow theory* [60] provides a suitable approximation for fluid–structure interactions. This approach models the interactions through a system of integro-differential equations in the time domain. If the floater position and orientation is defined by the pose vector $p : t \mapsto \mathbb{R}^6$, the equation of motion is expressed through the following function Γ, written, for $t \in \mathbb{R}^+$, as follows

$$\Gamma : \begin{cases} \mathcal{M}\dot{\nu} = f_e + f_h + f_r, \\ \nu = \dot{p}, \end{cases} \tag{1}$$

where $\mathcal{M} \in \mathbb{R}^{6\times6}$ encloses the contribution of the floater inertia tensor $M_f \in \mathbb{R}^{6\times6}$ and the added mass at infinite frequency $m^\infty \in \mathbb{R}^{6\times6}$, *i.e.* $\mathcal{M} = (M_f + m^\infty)$, $f_h \in \mathbb{R}^6$ is the hydrostatic force, directly proportional to the position vector p, through the hydrostatic stiffness matrix $s_h \in \mathbb{R}^{6\times6}$, and $f_e \in \mathbb{R}^6$ is the wave excitation force [61,62]. Moreover, the radiation force f_r, that accounts for the dissipative hydrodynamic effects, is defined by a convolution integral through the Cummins equation, involving a corresponding radiation kernel $k_r \in \mathbb{R}^{6\times6}$ and velocity vector $\nu = \dot{p}$ [63,64].

2.2. Characterization of the reaction forces

Eq. (1) provides a description of the floater dynamics exclusively considering the fluid–structure interaction. Hence, an analysis on the loads acting on the inner bodies, responsible for the overall energy generation process, is effectively required. To facilitate the computation and understanding of the system, the study of IRM WECs can be divided into two sub-problems: Computation of the reaction force vector and

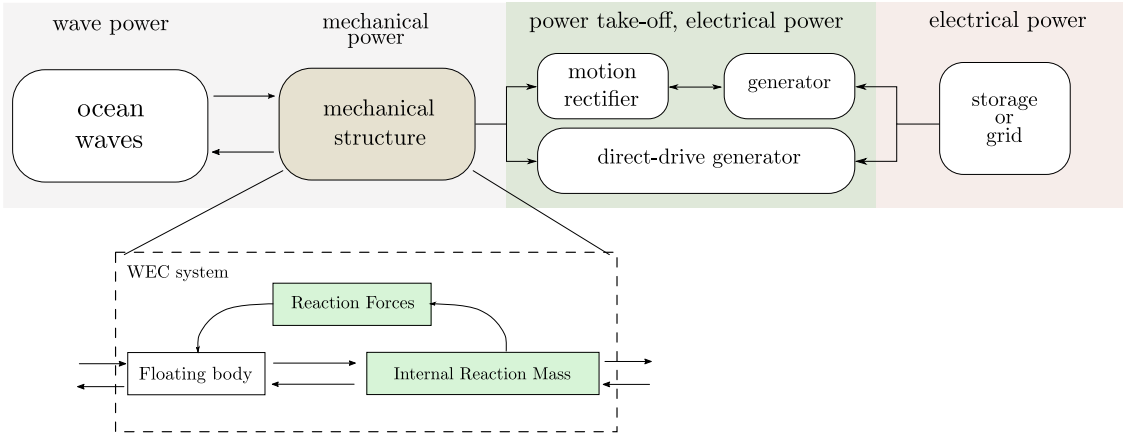

Fig. 2. Schematic representation of an IRM WEC energy transformation process, highlighting the conversion from ocean wave power to grid-compatible electric energy. The diagram illustrates the transformation process through mechanical power development, which depends on the interaction between the floater and the reacting system, and the electrical power generation dependent on the PTO nature.

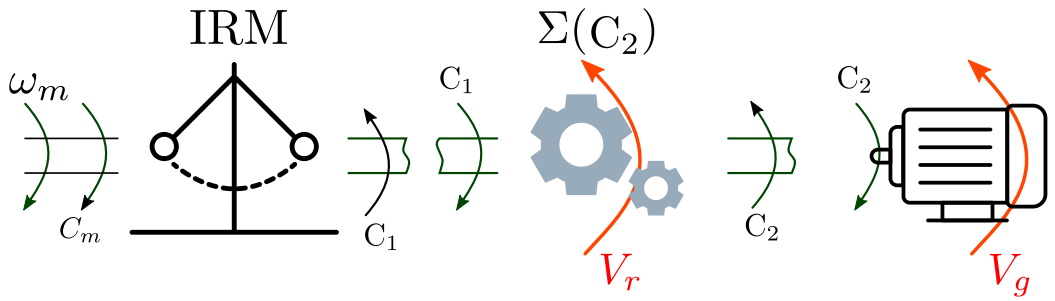

Fig. 3. Schematic representation of the load distribution along the PTO transmission axis, from the torque generated by the floater (prime mover torque) to the reaction torque exerted by the reacting system on the floater.

formulation of the dynamical equation describing the motion of the reacting mass-related DoF.

The reacting systems usually have a single associated DoF, and therefore are allowed to rotate with respect to the PTO axis, alternatively to slide on a plane, but are constrained with respect to the remaining set of motions. To begin we define a generic generalized coordinate $\rho : \mathbb{R}^+ \to \mathbb{R}, t \mapsto \rho$, which is related to the IRM DoF. A reaction force vector $f_{rc} \in \mathbb{R}^6$ is exerted following the relation

$$f_{rc} = M_m \ddot{p} + I_{mf} \ddot{\rho} - f_{bk}, \tag{2}$$

where $M_m : \mathbb{R}^+ \to \mathbb{R}^{6\times6}$ is the generalized mass-inertia matrix of the inertial reacting system, $I_{mf} \in \mathbb{R}^6$ is the inertia vector coupling the PTO DoF to the floater, and $f_{bk} : \mathbb{R}^+ \to \mathbb{R}^6$ encloses all the reacting effects both due to Coriolis and centrifugal forces, and effects due to gravity.

A focused discussion is necessary for the study of the PTO-related DoF. With reference to Fig. 3, the torque activating the energy extraction axis is $C_m : \mathbb{R}^+ \to \mathbb{R}$, which excites the inertial mass, since its motion is not constrained (although it is coupled with a PTO system, which is rigidly connected to the floater). Nevertheless, keeping the dynamic equilibrium on the transmission shaft results in the generation of a reaction force $V_{tot} : \mathbb{R}^+ \to \mathbb{R}$ transmitted to the floater through the support frame. Note that V_{tot} is defined as the sum of the reaction forces $V_r : \mathbb{R}^+ \to \mathbb{R}$ and $V_g : \mathbb{R}^+ \to \mathbb{R}$, transmitted to the floater through the PTO frame conditioning stage and the generator, respectively, hence

$$V_{tot} = V_r + V_g. \tag{3}$$

Specifically, the reaction forces exerted on the floater, attributed to the PTO stage, are defined as the difference between the input torque C_1 and the output torque C_2 ($V_r = C_1 - C_2$). C_2 corresponds to the control function, while the former depends on the specific PTO stage, which can be direct-drive, either mechanical or hydraulic [65,66]. Therefore, it can be generally expressed as $C_1 = \Sigma(C_2)$, with the operator Σ defined according to the type of PTO adopted. For instance, for a mechanical PTO system, based on a gear stage, $C_1 = \eta_{gb} C_2$, where $\eta_{gb} \in \mathbb{Z}^+$ is the gearbox reduction parameter. Knowing that the generator transmitted reaction force is exactly the control force C_2 ($V_g = C_2$), the following is implied:

$$V_{tot} = C_1. \tag{4}$$

Hence, the dynamical equation that describes the motion of the IRM WEC system, through its rotational velocity $\omega_m \in \mathbb{R}$, is defined through the function $g : \mathbb{R}^+ \to \mathbb{R}^6$, $t \mapsto g$, is defined as follows

$$g : I_m \dot{\omega}_m = C_m - C_1 = C_m - \Sigma(C_2), \tag{5}$$

where I_m is the mass inertia with respect to the rotation axis. For sake of completeness, note that the extracted mechanical power $P_a \in \mathbb{R}$ is defined as the product between the control torque C_2 and the rotational velocity of the generator side, hence:

$$P_a = C_2 \Sigma^{-1}(\omega_m) \Rightarrow P_a = C_1 \omega_m. \tag{6}$$

2.3. Coupled mechanical-hydrodynamic model

With reference to the previous sections, specifically Eqs. (1), (2) and (5), we define the overall equation of motion of a generic IRM WEC. In particular, the wave force f_e, which is exogenous, induces the motion of the floater. The floater, influenced by hydrodynamic forces such as f_r and f_h, induces vibrations on the inner mechanical system. It behaves as a parametrically excited vibratory entity, as it is coupled with the floater and controlled by the PTO action C_1. A representation of the IRM WEC simulation loop is schematized in Fig. 4. However, due to partial constraints to the hull, the inertial mechanism generates reaction forces that are then applied back to the floating body.

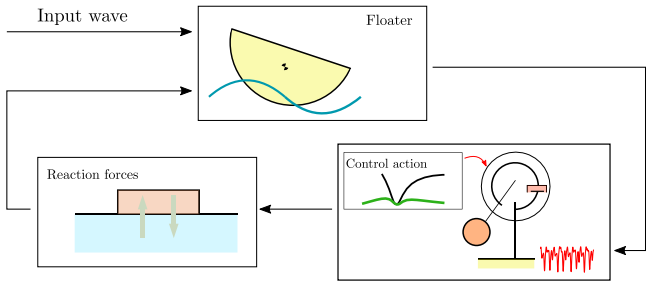

Fig. 4. Schematic representation of an IRM WEC simulation loop, encompassing the input wave and main simulation blocks. These blocks include the floater, which activates the inertial mechanism. The control action influences the set of reaction forces, which, together with the input wave, impact the floater dynamics.

Within this section, we provide the coupled mechanical-hydrodynamic model Γ', by considering the inherent mechanical coupling between the mechanism and the floater, and the hydrodynamic motion of the device activated by the wave input force, *i.e.*

$$\Gamma' : \begin{bmatrix} \mathcal{M} + M_m & I_{mf} \\ I_{fm} & I_m \end{bmatrix} \begin{bmatrix} \ddot{p} \\ \ddot{\rho} \end{bmatrix} = \begin{bmatrix} f_e + f_h + f_r + f_{bk} \\ C_m - C_1 \end{bmatrix}, \tag{7}$$

where $I_{mf} = I_{fm}^{\mathsf{T}}$ is the coupling vector linking the floater acceleration to the inertial effect on the IRM DOF. As highlighted in Eq. (7), the IRM WEC dynamics involve hydrodynamic modeling, the wave environment representation through the function f_e [67,68], the simulation of the PTO transformation function, and the mechanical coupling. It is worth highlighting that such a general scheme can be adapted according to the wave environmental conditions and by changing the definition of the PTO system. The latter can be tuned through the general function Σ, knowing that its effect on the mechanical system dynamics is defined by C_1, according to the generator exerted torque C_2.

However, this study specifically focuses on modeling the mechanical interaction, which includes determining the prime mover torque C_m, analyzing reaction forces transmitted from the inner mass to the floater (denoted as f_{bk}), and assessing inertial couplings, such as M_m, I_{m_f}, and I_{fm}.

Although the general scheme is presented in Eq. (7), a further nonlinear force F_{nl} can be added to the PTO DoF if a nonlinear stiffness mechanism is introduced. For instance, as demonstrated in [69,70] a spring attached to the mass can emulate a nonlinear varying recall force dependent on the pendulum's rotation angle [71]. These mechanisms aim to exploit bistability effects in wave energy systems [72,73]. It is crucial to note that if a nonlinear force acts on the PTO DoF according to the $\mathcal{R}(\mathcal{G}\xi\eta\zeta)$ frame, the corresponding reaction force on the floater must be defined using the transformation matrix mapping procedure. The literature analysis of gross output power indicates that rotating motion, whether chaotic or periodic, enhances energy harvesting performance by increasing power and broadening the system operating bandwidth [74]. On this scenario, nonlinear energy harvesting methods have been proposed, including nonlinear stiffness and nonlinear damping, acting even on raft-type WEC systems [75,76].

3. Dynamic modeling of the mechanical couplings

This section provides a clear derivation and analysis of the mechanical interaction between the floater and the IRM. The discussion is intentionally kept general, in order to introduce a versatile framework that can be easily adjusted with minor modifications, to accurately capture and represent the mechanical interaction for a wide family of devices. The proposed modeling procedure begins with the computation of the matrix that characterizes the kinematic chain of the mechanism: This includes the corresponding Jacobian matrix, which maps the system velocity from the inertial frame to the mechanism-fixed frame. Subsequently, the velocities of the bodies are directly formulated, allowing for the calculation of both kinetic and potential energy. In particular, starting with the kinematic characterization of the bodies involved, Section 3.1 introduces the reference frame to be set. Moreover, Section 3.2 describes the kinematic chain mapping the floater velocity from the inertial frame to the IRM-fixed reference frame, while Section 3.3 states the overall velocity vector of the reacting mass.

3.1. Reference frames definition

During operations, the dynamics of an IRM WEC device involve the mechanical interaction between two bodies: the floater and an inertial reacting system. These two bodies are interconnected and influence each other motion and behavior. Both of them need to be defined in relation to an inertial reference frame. This is achieved by using a set of generalized coordinates that captures the motion and behavior of virtual joints. The generalized coordinates are defined according to the reference frames shown in Fig. 5. In particular, a vertical axis pendulum device, installed in an axial-symmetric floater, *e.g.* a spherical cup, is selected as a representative case-study. Note that, the vertically-hinged pendulum is the most relevant technological solution, hence it is adopted as a reference benchmark in the following preliminary computations. Therefore, according to Fig. 5, the following reference frames are subsequently introduced:

- The inertial frame $\mathcal{R}(OXYZ)$, whose origin coincide with O.
- The hull-fixed reference frame, denoted as $\mathcal{R}(\mathcal{O}'\text{xyz})$, is centered at the hull's center of gravity (CoG), marked as O'. The frame $\mathcal{R}(\mathcal{O}'\text{xyz})$ is capable of moving freely in space and accommodates the complete range of motions, including both linear and rotational movements. Specifically, the orientation of this frame is determined using the roll-pitch-yaw convention, which involves subsequent rotations relative to the axes in the order: z, y and x.
- The inertial reacting system motion is defined by the $\mathcal{R}(\mathcal{G}\Xi\mathcal{H}\mathcal{Z})$ frame, whose $\mathcal{Z}$-axis, for the specific case study of Fig. 5 is pointing upward, according to the PTO axis. The axis $\Xi\mathcal{H}\mathcal{Z}$ are always parallel to x, y, z-axis, but having the origin in $\mathcal{G}$. In particular, the position of $\mathcal{G}$ with respect to $\mathcal{R}(\mathcal{O}'\text{xyz})$ is determined by the vector $r = [x_0\ y_0\ z_0]$.
- $\mathcal{R}(\mathcal{G}\xi\eta\zeta)$ is the IRM-fixed reference frame. For instance, such a frame follows the vertically-hinged pendulum rotation with respect the ζ-axis.

It is worth noting that the kinematic characterization of each mechanism is closely interrelated, requiring the development of a generic scheme. The dynamics of the inner reacting mass, within the floater, are influenced by parametric excitation and external forces. While the latter can be defined by the user through a proper control algorithm, as discussed in [45,77,78], the parametric excitation is inherently linked to the hull motion, which activates the entire energy transformation process. Specifically, the motion of the floater, and its derivatives, significantly affects the IRM motion. Meanwhile, the interaction between DoF varies depending on the type of mechanism selected for the WEC. In details, the position and orientation of the floater in the inertial reference frame, is indicated by the vector $p = \left[X^{\mathsf{T}}\ \Phi^{\mathsf{T}}\right]^{\mathsf{T}}$, whose vector $X = [x\ y\ z]^{\mathsf{T}} \in \mathbb{R}^3$ establishes the surge, sway and heave motion of the floater, respectively, while the vector $\Phi = [\theta\ \delta\ \psi]^{\mathsf{T}} \in \mathbb{R}^3$ determines its roll, pitch and yaw rotation. When considering the reacting mass, an additional generalized coordinate is required, resulting in the definition of the 'augmented' vector $q = \left[p^{\mathsf{T}}\ \rho\right]^{T}$. Consequently, with the identification of the main bodies involved in the power conversion chain, we state the nonlinear set of differential equations, which describe the floater-mechanism interaction, in the following sections.

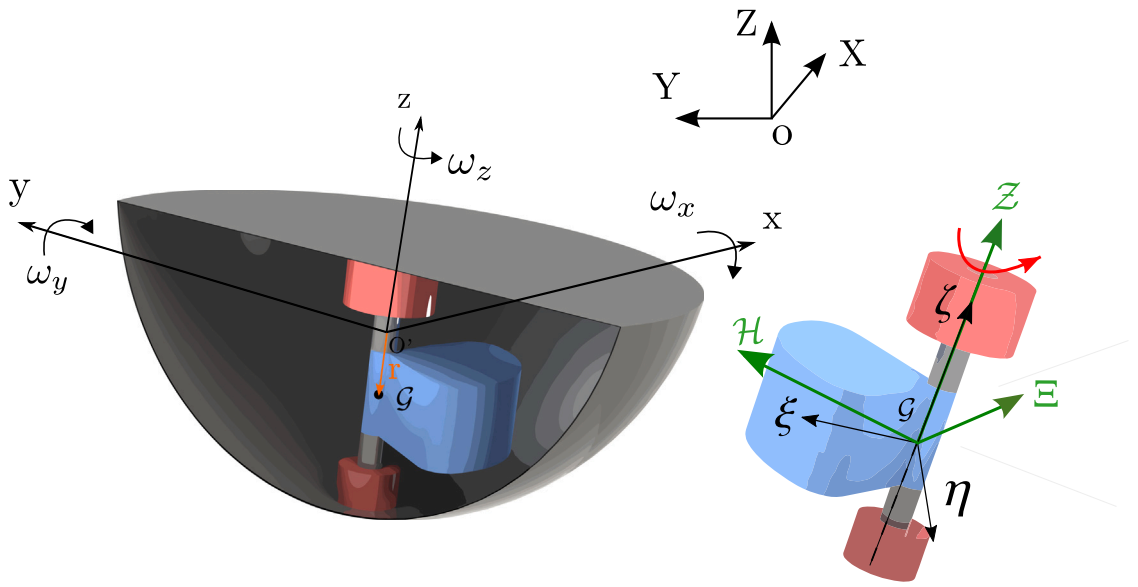

Fig. 5. Diagram illustrating the reference frame setup for IRM WECs, from the inertial frame to the reactive mass-fixed frame. It moves through the floater-fixed reference frames, one defined at the floater's CoG and the second at the inertial mass position.

3.2. Kinematics chain description

This section aims to define, unequivocally, the kinematics of the rigid body interconnected to the electric generator for the energy transformation process. Following a step-by-step procedure, the kinematic transformations in between the reference frames allow for the definition of the overall velocity of the inner reacting mass. For this purpose, an IRM WEC can be schematized as a chain of rigid links and joints. In particular, the inertial conversion unit can be represented through a translational or rotational joint, according to the adopted technological solution. As previously discussed, for technological constraints, the IRM has a single DoF, *i.e.* $m = 1$, which is coupled with the PTO system. The number of DoFs can be increased, as in the case of the gimbaled pendulum, where the mass motion is described by a set of two joints.

Furthermore, the floater can be modeled as a 6 DoF joint, *i.e.* it is allowed to move in space and rotate with respect to the x-, y- and z-axis. For instance, the velocity mapping from the inertial frame $\mathcal{R}(OXYZ)$ to the floater frame $\mathcal{R}(\mathcal{O}'\text{xyz})$ is the first transformation to be defined. Subsequently, the velocity is transported on $\mathcal{R}(\mathcal{G}\Xi\mathcal{H}\mathcal{Z})$ frame, under the assumption that the origin $\mathcal{O}'$ of the $\mathcal{R}(\mathcal{O}'\text{xyz})$ frame does not lie on the line defining the energy transmission axis toward the PTO system. Finally, the velocity projection from the $\mathcal{R}(\mathcal{G}\Xi\mathcal{H}\mathcal{Z})$ frame into the IRM-fixed reference frame $\mathcal{R}(\mathcal{G}\xi\eta\zeta)$ is required, since a further DoF is added by the mechanism itself.

The floater velocity vector $V_{f_{xyz}} = [v_x\ v_y\ v_z]^\mathsf{T}$, where v_x, v_y and v_z are surge, sway, and heave velocities defined in the floater reference frame $\mathcal{R}(\mathcal{O}'\text{xyz})$, is obtained through a kinematic transformation from the vector $\dot{X}$. Such linear vector projection involves a set of three transformations, characterized by roll, pitch and yaw rotations, incorporated into the matrix $C \in \mathbb{R}^{3\times3}$, whose transpose is explicitly defined as follows

$$C^\mathsf{T} = R(\theta, \hat{\imath})^\mathsf{T} R(\delta, \hat{\jmath})^\mathsf{T} R(\psi, \hat{k})^\mathsf{T}. \tag{8}$$

About the rotational velocity, it is well known that the velocity vector in the body-frame, *e.g.* $\mathcal{R}(\mathcal{O}'\text{xyz})$, does not correspond to the derivative of the generalized coordinates vector Φ. For instance, the computation of ω_x, ω_y and ω_z, the angular velocities defined in the floater-fixed reference frame $\mathcal{R}(\mathcal{O}'\text{xyz})$, is dependent on the analytical Jacobian $D \in \mathbb{R}^{3\times3}$. On this purpose, the analytical Jacobian matrix $J_F \in \mathbb{R}^{6\times6}$, which links the vector of the derivative of generalized coordinates to the floater velocity, defined in the body frame, is explicitly stated as follows

$$w_{xyz} = \begin{bmatrix} V_F \\ \Omega_F \end{bmatrix} = J_F\, \dot{p} = \begin{bmatrix} C^\mathsf{T} & 0 \\ 0 & D \end{bmatrix} \begin{bmatrix} \dot{X} \\ \dot{\Phi} \end{bmatrix}. \tag{9}$$

Furthermore, the velocity vector $w_{\Xi\mathcal{H}\mathcal{Z}} = [V_M^\mathsf{T}\ \ \Omega_M^\mathsf{T}]^\mathsf{T}$, defined in $\mathcal{R}(\mathcal{G}\Xi\mathcal{H}\mathcal{Z})$, considering the position of the origin $\mathcal{G}$ with respect to $\mathcal{O}'$ dependent on the position vector r, is expressed through the following relation

$$w_{\Xi\mathcal{H}\mathcal{Z}} = \begin{bmatrix} V_M \\ \Omega_M \end{bmatrix} = J_M\, \dot{p} = \begin{bmatrix} C^\mathsf{T} & -\tilde{r}D \\ 0 & D \end{bmatrix} \begin{bmatrix} \dot{X} \\ \dot{\Phi} \end{bmatrix}, \tag{10}$$

where $J_M \in \mathbb{R}^{6\times6}$ is the Jacobian matrix linking $\dot{p}$ to $w_{\Xi\mathcal{H}\mathcal{Z}}$. The Jacobian J_M in Eq. (10) can be written in, compact form, using the fact that the velocity V_M of a generic point in a rigid body is defined as

$$V_M = V_F + \Omega_M \times r = V_F + \tilde{\Omega}_M r = V_F - \tilde{r}\Omega_M. \tag{11}$$

Please note that an additional transformation is necessary to express the IRM WEC velocity in the mechanism-fixed reference frame $\mathcal{R}(\mathcal{G}\xi\eta\zeta)$, whose dynamics are described by the generalized coordinates ρ. The specific definition of the coordinate ρ is contingent upon the nature of the chosen inertial reacting device, *i.e.* rotating or sliding, as discussed in the following.

Rotating inertial reacting system. For rotation-based mechanical systems, such as the case of pendulums and gyroscopes, a further rotation is necessary for the velocity vector to be defined into $\mathcal{R}(\mathcal{G}\xi\eta\zeta)$. The additional coordinate ρ represents an angle, characterized, in this general context, by means of three canonical angles α, β, and γ, whose association to a specific IRM depends on the orientation of the rotation axis, whether vertical or horizontal. The rotation matrix associated to ρ is generally referred to as $\mathcal{R}_u \in \mathbb{R}^{3\times3}$.

The kinematic link matrix, which maps the generalized velocity vectors $\dot{X}$ and $\dot{\Phi}$ into the mechanism-based velocity V_G and Ω_G, for rotational mechanisms, termed J_G, is defined as follows

$$J_G = \begin{bmatrix} \mathcal{R}_u C^\mathsf{T} & -\mathcal{R}_u \tilde{r} D \\ 0 & \mathcal{R}_u D \end{bmatrix}, \tag{12}$$

and the following holds

$$\begin{bmatrix} V_G \\ \Omega_G \end{bmatrix} = \begin{bmatrix} \mathcal{R}_u C^\mathsf{T} & -\mathcal{R}_u \tilde{r} D \\ 0 & \mathcal{R}_u D \end{bmatrix} \begin{bmatrix} \dot{X} \\ \dot{\Phi} \end{bmatrix}. \tag{13}$$

Up to this point, the velocity of the floater is projected onto the reference frame of the mechanism. However, the proper velocity of PTO system is required to be added to the projected floater velocity. These are subjected to its own rotational velocity $\omega_m \in \mathbb{R}^3$, and then total rotational velocity vector Ω_I is computed through the following equation:

$$\Omega_I = \Omega_G + \omega_m. \tag{14}$$

The total system velocity $w_{\xi\eta\zeta} = [V_I^\top \ \Omega_I^\top]^\top$ expressed in the $\mathcal{R}(\mathcal{G}'\xi\eta\zeta)$ frame is stated through the matrix J_I

$$J_I = \begin{bmatrix} \mathcal{R}_u C^\top & -\mathcal{R}_u \tilde{r} D & 0 \\ 0 & \mathcal{R}_u D & \mathcal{D}_u \end{bmatrix}, \tag{15}$$

and hence the following relation

$$\begin{bmatrix} V_I \\ \Omega_I \end{bmatrix} = \begin{bmatrix} \mathcal{R}_u C^\top & -\mathcal{R}_u \tilde{r} D & 0 \\ 0 & \mathcal{R}_u D & \mathcal{D}_u \end{bmatrix} \begin{bmatrix} \dot{X} \\ \dot{\boldsymbol{\Phi}} \\ \dot{\rho} \end{bmatrix}, \tag{16}$$

holds, where $\mathcal{D}_u \in \mathbb{R}^{3\times m}$ is defined in terms of the basis vector e_i^3 for a single-DoF mechanism, *e.g.* $\mathcal{D}_u = e_3^3 = [0 \quad 0 \quad 1]^\top$ for the vertical-axis pendulum system of Fig. 5. It is worth noting that $V_I = [v_\xi \ v_\eta \ v_\zeta]^\top$, whose elements are v_ξ, v_η and v_ζ, and the angular velocity vector $\Omega_I = [\omega_\xi \ \omega_\eta \ \omega_\zeta]^\top$, defined by the components ω_ξ, ω_η and ω_ζ, are the linear and angular velocity vectors, respectively, defined with respect to the $\mathcal{R}(\mathcal{G}\xi\eta\zeta)$ frame.

For a multi-DoF mechanical component, *e.g.* the gimbaled pendulum, where $\rho = [\alpha \ \beta]$, the block matrices $\mathcal{R}_u$ and D_u in Eq. (16) are distinctly defined. Their characterization takes it account that two consecutive rotation, α and β, occur with respect t the ξ- and η- axis, respectively. In particular, the rotation matrix is consequently stated as $\mathcal{R}_u = \mathcal{R}_\beta^\top \mathcal{R}_\alpha^\top$, while $\mathcal{D}_u$ is defined as follows

$$\mathcal{D}_u = \begin{bmatrix} \cos\beta & 0 \\ 0 & 1 \\ \sin\beta & 0 \end{bmatrix}. \tag{17}$$

Sliding reacting system. These systems are subjected to their linear velocity $v_m \in \mathbb{R}^3$, and then the total linear velocity vector V_I is computed through the following equation:

$$V_I = V_M + v_m. \tag{18}$$

The Jacobian matrix $J_I \in \mathbb{R}^{6\times(6+m)}$ for sliding mechanism is then computed as

$$\begin{bmatrix} V_I \\ \Omega_I \end{bmatrix} = \begin{bmatrix} C^\top & -\tilde{r} D & e_i^3 \\ 0 & D & 0 \end{bmatrix} \begin{bmatrix} \dot{X} \\ \dot{\boldsymbol{\Phi}} \\ \dot{\rho} \end{bmatrix}. \tag{19}$$

To sum up, the system velocity is defined through an associated Jacobian matrix, which states a precise relation between the set of generalized coordinates and the velocity into the mechanism frame. To streamline the procedure, the characterization of the velocity into the mechanism reference frame starts with the projection of the floater velocity vector in the body frame, through the matrix J_F. While the matrix J_M allows a further velocity representation with respect to the rotation axis, then allowing the following mapping $\mathcal{R}(\mathcal{O}'xyz) \mapsto \mathcal{R}(\mathcal{G}\Xi\mathcal{H}\mathcal{Z})$ to encompass the velocity projection from the floater frame to the IRM reference position, defined by the r vector. Conversely, the matrices J_G and J_I are responsible for incorporating the additional DoF from the IRM. These matrices project the floater's velocity into the $\mathcal{R}(\mathcal{G}\xi\eta\zeta)$ frame using the rotation matrix associated with the IRM's generalized coordinates. This process is used exclusively for rotating systems, such as pendulums and gyroscopes. Additionally, a block matrix is added to incorporate the contribution of the mechanism velocity. The reader can refer to Table 2 for a summary of the Jacobian matrices required during the main transformation steps.

3.3. End-effector velocity

As discussed previously within this section, every mechanical IRM system can be modeled as an assembly of several rigid bodies. Therefore, the spatial velocity vector $[V_{EF} \ \Omega_{EF}]^\top$ must be defined, where $V_{EF} \in \mathbb{R}^3$ and $\Omega_{EF} \in \mathbb{R}^3$ represent linear and angular velocities of each single body, respectively. In particular, these depend on the architecture of the selected mechanism hence, in the following, we define the end-effector velocity for the three main subfamilies of IRM systems considered: gyroscopes, pendulum, and sliding mass. The reader can refer to Table 3 for further details.

Gyroscope. A gyroscope system consists of two main components: the gimbal and the flywheel. The velocity vector of the gimbal corresponds to the ne described by Eq. (16). However, the flywheel experiences an additional velocity, *i.e.* its spinning velocity about its polar axis, denoted as $\dot{\varphi}$. Therefore, the angular velocity component of the flywheel $\omega_{\text{fw}} = e_m^3 \dot{\varphi}$, where m depends on the versor orientation, knowing it has to be parallel to the flywheel polar axis. Without loss of generality the following relation holds:

$$\Omega_{EF} = \Omega_I + \omega_{\text{fw}}. \tag{20}$$

Pendulum. For pendulum-based systems, although the angular velocity is invariant with respect Ω_I, the linear velocity V_{EF} is defined according to the position vector of the pendulum mass with respect to the $\mathcal{R}(\mathcal{G}'\xi\eta\zeta)$ frame, through the vector r_m, *i.e.*

$$V_{EF} = V_I + \tilde{\Omega}_I r_m. \tag{21}$$

In particular, r_m can be defined differently according to the orientation of the swinging mass. For horizontal pendulum-based devices, the arm vector is $r_{m_h} = [0 \ 0 \ -l_p]^\top$, where l_p is the length of the link defined from the ξ-axis for a horizontal-axis pendulum and gimbaled pendulum while, for the vertical pendulum, $r_{m_v} = [l_p \ 0 \ 0]^\top$, where l_p is the distance between the vertical axis ζ and the mass CoG, knowing that the pendulum mass lies on the ξ-axis.

Sliding mass. In a sliding mass system, the end effector's velocity is dependent on the generalized coordinate itself. Specifically, the rotation velocity of the sliding mass corresponds to the velocity vector Ω_I, and the linear velocity is described by Eq. (21). Additionally, the mass position is instantaneously changing in time, since it is defined by the coordinate ρ. For instance, for the horizontal sliding body the position vector is $r_{m_h} = [\alpha \ 0 \ 0]$, while for the vertical configuration, it is $r_{m_v} = [0 \ 0 \ \gamma]$.

4. Computation of the dynamic equation of IRM WECs

From the definition of an appropriate set of reference frames to properly describe system motion, this section introduces the procedure for the derivation of the mathematical model characterizing such devices, focusing on the derivation of the coupling between the floater and the associated PTO system, mainly governed by nonlinear effects such as centrifugal and Coriolis forces. The resulting nonlinear model allows for the evaluation of WEC performance with high fidelity, providing detailed insights into its behavior. Furthermore, the nonlinear model serves as a foundation for developing a linear counterpart. Such a linear model offers simplicity, facilitating the study of the system and the assessment of its dynamic performance, as well as design and synthesis of real-time energy-maximizing control technology. For this purpose, Section 4.1 states the Euler equations for defining the floater's motion in 6 DoF, and Section 4.2 addresses the analytical expression for the reaction mass dynamics and the definition of the reaction forces.

Table 2
Jacobian matrix for transforming from $\mathcal{R}(OXYZ)$ to $\mathcal{R}(\mathcal{G}\xi\eta\zeta)$.

Reference frame transformation	Jacobian matrix
$\mathcal{R}(OXYZ) \mapsto \mathcal{R}(\mathcal{O}'\text{xyz})$	$J_F = \begin{bmatrix} C^\top & 0 \\ 0 & D \end{bmatrix}$
$\mathcal{R}(\mathcal{O}'\text{xyz}) \mapsto \mathcal{R}(\mathcal{G}\Xi\mathcal{H}\mathcal{Z})$	$J_M = \begin{bmatrix} C^\top & -\tilde{r}D \\ 0 & D \end{bmatrix}$
$\mathcal{R}(\mathcal{G}\Xi\mathcal{H}\mathcal{Z}) \mapsto \mathcal{R}(\mathcal{G}\xi\eta\zeta)$	$J_I = \begin{bmatrix} \mathcal{R}_u C^\top & -\mathcal{R}_u \tilde{r} D & 0 \\ 0 & \mathcal{R}_u D & \mathcal{D}_u \end{bmatrix} \qquad J_I = \begin{bmatrix} C^\top & -\tilde{r}D & e_i^3 \\ 0 & D & 0 \end{bmatrix}$

4.1. Floater dynamics and reaction forces

The mechanical power transmitted from the wave to the IRM system, through the floater motion, is converted into electric power by a suitable control action exerted by the PTO system. The power output of a wave energy device is then ultimately integrated into the grid through power converters and an associated conditioning process [79]. On the basis of this, the focus is now dedicated to the first body (primary mover) acting as part of such process, *i.e.* the floater. Let $m_f \in \mathbb{R}^+$ and $I_f = diag([I_x\ I_y\ I_z])$, with $I_x, I_y, I_z \in \mathbb{R}^+$, be the mass and inertia matrix of a generic floater. Then, the dynamic equations in 6 DoFs with respect to the body axis can be expressed through the Euler equation. For further details the reader can refer to Appendix A. In particular the equation describing the floater dynamics can be rewritten as follows:

$$M_F \dot{w}_{xyz} + B_F(w_{xyz}) w_{xyz} = F_{ext}, \tag{22}$$

where $w_{xyz} = [v_x\ v_y\ v_z\ \omega_x\ \omega_y\ \omega_z]^\top$ is the floater velocity vector in the floater-fixed reference frame and $F_{ext} \in \mathbb{R}^6$ is the generalized external force vector. Note that the velocity vector and its derivative $\dot{w}_{xyz}$ are defined with respect to the vector of generalized coordinates p, *i.e.*

$$\begin{cases} w_{xyz} = J_F\, \dot{p}, \\ \dot{w}_{xyz} = \dot{J}_F\, \dot{p} + J_F\, \ddot{p}. \end{cases} \tag{23}$$

This can be used to compute, in compact form, the dynamics into the inertial reference frame $\mathcal{R}(OXYZ)$:

$$M_f(p)\ddot{p} + B_f(p, \dot{p})\dot{p} = f_{ext}, \tag{24}$$

where $f_{ext} \in \mathbb{R}^6$ is the vector of external forces expressed in the inertial frame, and the matrices $M_f(p) : p \mapsto M_f$ and $B_f(p, \dot{p}) : \{p, \dot{p}\} \mapsto B_f$ are

$$\begin{cases} M_f = J_F^\top M_F J_F, \\ B_f = J_F^\top M_F \dot{J}_F + J_F^\top B_F J_F, \end{cases} \tag{25}$$

allowing (24) to be explicitly rewritten as

$$J_F^\top M_F J_F \ddot{p} + (J_F^\top M_F \dot{J}_F + J_F^\top B_F J_F)\dot{p} = f_{ext}. \tag{26}$$

4.2. Lagrange equation defined for quasi-coordinates

Even the dynamic coupling between the two bodies happens through the identification of the reaction forces, which can be a key factor for determining the design of the mechanical components. This section characterizes such reaction forces, and compute the overall system dynamics, where all the main effects are enclosed into a compact differential equation, based on the previous derivations. In particular, the computation of the dynamic equation of the system is derived via a Lagrangian approach, defined for quasi-coordinates.

For a multi-DoF IRM device, the development of a set of equations, based on quasi-coordinates, can be more convenient than a system representation via generalized coordinates [80]. Since the relative motion between floater and internal mechanism is effectively exploited during the device operating condition, the quasi-coordinates, or pseudo-coordinates, allow to solve the dynamic problem on the PTO-fixed frame, *i.e.* $\mathcal{R}(\mathcal{G}\xi\eta\zeta)$. Fr instance, knowing the generalized coordinate vector $p(t)$, the quasi-coordinates (or pseudo-coordinates) of the IRM WEC under study [81] are the velocity vectors V_I and Ω_I, defined in Eqs. (16) and (19), respectively. These are used to define the force and moment equations in the reacting mass fixed-frame, *i.e.* about the axes ξ, η, ζ, simplifying the computation of the dynamic equations for this family of systems. In particular, the Lagrange equations for quasi-coordinates are expressed in Appendix B. Therefore, in the $\mathcal{R}(\mathcal{G}\xi\eta\zeta)$ frame the following differential equation holds

$$M_I \dot{w}_{\xi\eta\zeta} + B_I(w_{\xi\eta\zeta}) w_{\xi\eta\zeta} + G_{\xi\eta\zeta} = F_{rc}, \tag{27}$$

where $M_I \in \mathbb{R}^{6\times6}$ and $B_I(w_{\xi\eta\zeta}) \in \mathbb{R}^{6\times6}$ are the mass and damping matrix respectively, defined in the IRM-fixed reference frame, where the latter encloses all the nonlinear effects, such as the Coriolis and centrifugal forces. Moreover, $G_{\xi\eta\zeta} \in \mathbb{R}^6$ includes all the effects of the gravity on the mechanism, and it is derived from the potential energy computation, ad detail in Appendix B, and $F_{rc} = [F_g\ T_g]^\top$ is the reaction force vector, and $F_g \in \mathbb{R}^3$ and $T_g \in \mathbb{R}^3$ represent linear and angular components, respectively. Additionally, F_{rc} is defined as:

$$F_{rc} = \begin{bmatrix} F_\xi & F_\eta & F_\zeta & T_\xi & T_\eta & T_\zeta \end{bmatrix}^\top. \tag{28}$$

We do note that, the Equation presented in (27), can be written in compact form, referred to the inertial reference frame, into the generalized coordinate-space:

$$M_i(q)\ddot{q} + B_i(q, \dot{q})\dot{q} + G(q) = \bar{f}_{rc}, \tag{29}$$

where $M_i \in \mathbb{R}^{7\times7}$, $B_i \in \mathbb{R}^{7\times7}$ are the mechanism system matrices written in the inertial space. Moreover, $G(q) : \mathbb{R}^7 \to \mathbb{R}^7, q \mapsto G(q)$ is the function defining the gravity effect, and $\bar{f}_{rc} = [f_{rc}^\top\ C_1]^\top$ is the augmented reaction force vector, which includes the corresponding PTO control action. Note that Eq. (29) is obtained through the following relations

$$\begin{cases} M_i(q) = J_I^\top M_I J_I, \\ B_i(q) = J_I^\top M_I \dot{J}_I + J_I^\top B_M J_I. \end{cases} \tag{30}$$

Therefore, substituting Eq. (30) into (29), the equation characterizing the reaction forces is the following:

$$J_I^\top M_I J_I \ddot{q} + J_I^\top M_I \dot{J}_I \dot{q} + J_I^\top B_I J_I \dot{q} + G(q) = \bar{f}_{rc}. \tag{31}$$

To streamline the exposition, the derivatives of the block matrices composing the Jacobians are presented in the Appendix C. Finally, such reaction forces are required to be coupled with the floater dynamics, stated in Eq. (26), recalling that the coupling on the PTO axis is described by Eq. (3). Additionally, $\bar{f}_{rc_m}$ is defined:

$$\bar{f}_{rc} = J_I^\top F_{rc} = \begin{bmatrix} f_x & f_y & f_z & f_\theta & f_\delta & f_\psi & C_1 \end{bmatrix}^\top. \tag{32}$$

Finally, the nonlinear expressions for mass matrices and reaction forces, presented in Eq. (7), are defined in the following expression

$$\begin{aligned} \begin{bmatrix} f_{bk} \\ C_m \end{bmatrix} &= (J_I^\top M_I \dot{J}_I + J_I^\top B_I J_I)\dot{q} - G(q), \\ \begin{bmatrix} M_m & I_{mf} \\ I_{fm} & I_m \end{bmatrix} &= J_I^\top M_I J_I. \end{aligned} \tag{33}$$

Table 3
Jacobian matrix and end-effector velocity definition.

IRM device	Reference frame	Jacobian	Velocity vector
Pendulum: vertical axis	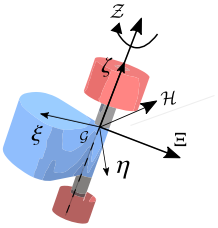	$J_I = \begin{bmatrix} \mathcal{R}_\gamma^\top C^\top & -\mathcal{R}_\gamma^\top \tilde{r} D & 0 \\ 0 & \mathcal{R}_\gamma^\top D & e_3^3 \end{bmatrix}$	$\begin{bmatrix} V_{EF} \\ \Omega_{EF} \end{bmatrix} = \begin{bmatrix} V_I \\ \Omega_I \end{bmatrix} + \begin{bmatrix} 0 & \tilde{\Omega}_I \\ 0 & 0 \end{bmatrix} \begin{bmatrix} 0 \\ r_{m_v} \end{bmatrix}$
Pendulum: horizontal axis	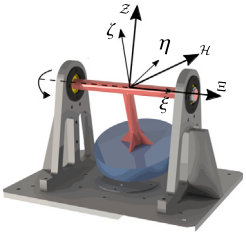	$J_I = \begin{bmatrix} \mathcal{R}_\alpha^\top C^\top & -\mathcal{R}_\alpha^\top \tilde{r} D & 0 \\ 0 & \mathcal{R}_\alpha^\top D & e_1^3 \end{bmatrix}$	$\begin{bmatrix} V_m \\ \Omega_m \end{bmatrix} = \begin{bmatrix} V_I \\ \Omega_I \end{bmatrix} + \begin{bmatrix} 0 & \tilde{\Omega}_I \\ 0 & 0 \end{bmatrix} \begin{bmatrix} 0 \\ r_{m_h} \end{bmatrix}$
Gimbaled pendulum	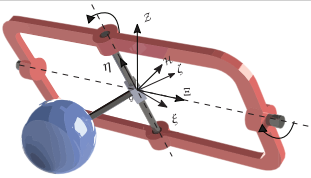	$J_I = \begin{bmatrix} \mathcal{R}_\beta^\top \mathcal{R}_\alpha^\top C^\top & -\mathcal{R}_\beta^\top \mathcal{R}_\alpha^\top \tilde{r} D & 0 \\ 0 & \mathcal{R}_\beta^\top \mathcal{R}_\alpha^\top D & D_u \end{bmatrix}$	$\begin{bmatrix} V_{EF} \\ \Omega_{EF} \end{bmatrix} = \begin{bmatrix} V_I \\ \Omega_I \end{bmatrix} + \begin{bmatrix} 0 & \tilde{\Omega}_I \\ 0 & 0 \end{bmatrix} \begin{bmatrix} 0 \\ r_{m_h} \end{bmatrix}$
Gyroscope: vertical axis	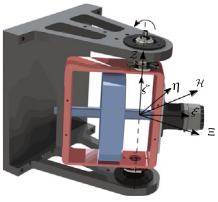	$J_I = \begin{bmatrix} \mathcal{R}_\gamma^\top C^\top & -\mathcal{R}_\gamma^\top \tilde{r} D & 0 \\ 0 & \mathcal{R}_\gamma^\top D & e_3^3 \end{bmatrix}$	$\begin{bmatrix} V_{EF} \\ \Omega_{EF} \end{bmatrix} = \begin{bmatrix} V_I \\ \Omega_I \end{bmatrix} + \begin{bmatrix} 0 \\ e_1^3 \dot{\varphi} \end{bmatrix}$
Gyroscope: horizontal axis	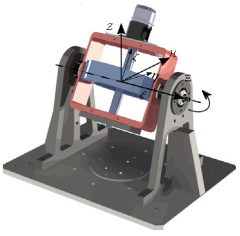	$J_I = \begin{bmatrix} \mathcal{R}_\alpha^\top C^\top & -\mathcal{R}_\alpha^\top \tilde{r} D & 0 \\ 0 & \mathcal{R}_\alpha^\top D & e_1^3 \end{bmatrix}$	$\begin{bmatrix} V_{EF} \\ \Omega_{EF} \end{bmatrix} = \begin{bmatrix} V_I \\ \Omega_I \end{bmatrix} + \begin{bmatrix} 0 \\ e_3^3 \dot{\varphi} \end{bmatrix}$
Sliding mass: vertical axis	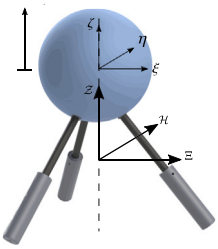	$J_I = \begin{bmatrix} C^\top & -^\top \tilde{r} D & e_3^3 \\ 0 & D & 0 \end{bmatrix}$	$\begin{bmatrix} V_{EF} \\ \Omega_{EF} \end{bmatrix} = \begin{bmatrix} V_I \\ \Omega_I \end{bmatrix} + \begin{bmatrix} 0 & \tilde{\Omega}_I \\ 0 & 0 \end{bmatrix} \begin{bmatrix} 0 \\ r_{m_v} \end{bmatrix}$
Sliding mass: horizontal axis	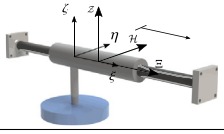	$J_I = \begin{bmatrix} C^\top & -\tilde{r} D & e_1^3 \\ 0 & D & 0 \end{bmatrix}$	$\begin{bmatrix} V_{EF} \\ \Omega_{EF} \end{bmatrix} = \begin{bmatrix} V_I \\ \Omega_I \end{bmatrix} + \begin{bmatrix} 0 & \tilde{\Omega}_I \\ 0 & 0 \end{bmatrix} \begin{bmatrix} 0 \\ r_{m_h} \end{bmatrix}$

Notably, Eq. (33) has been partially validated in a wave tank for a pitching floater coupled with a gyroscopic system, comparing the actual gyroscopic precession motion with the numerical one [82]. However, the validation of the reaction forces has been neglected, and due to the hydrodynamic properties of the floater, only a limited set of motion modes are coupled between the mechanical system and the floater, making this a very specific application case. Although this represents an initial validation attempt, deeper analyses are required. These are introduced through a case study in the following section.

5. A case study

We have conducted a very general approach for the definition of the mechanical interaction between the IRM and the floating body. In

this section, we describe the step-by-step computation of the reaction forces, going through the proposed framework, exploiting a guided case study, using the vertically-hinged pendulum system (presented in Fig. 5). Focusing on the case study, the kinematic matrices, kept general so far, is specifically expressed for the vertically hinged pendulum in Section 5.1. Section 5.2 presents its dynamic matrices, Section 5.3 introduces the linearization procedure and the statement of the linear matrices, and Section 5.4 introduces the main interacting modes of motion between the floater and the IRM, expanding the discussion to a wide family of WECs.

5.1. Vertically-hinged pendulum: kinematic transformation matrices

During operating conditions, the two rigid bodies involved in the dynamics of the vertically-hinged device are the floater and the pendulum mass, with the latter free to rotate with respect to a shaft, referenced to the former. The generalized coordinates are defined according to the reference frames shown in Fig. 5, recalling that these are placed respecting the rules presented in Section 3.1.

Recalling the floater pose vector p, as detailed in Section 3.1, the whole set of generalized coordinates is identifying adding the proper pendulum rotation angle γ, *i.e.* the following holds: $q = \begin{bmatrix} p^\top & \gamma \end{bmatrix}^T$. The characterization of J_I plays a crucial role for the solution of the system dynamics, recalling that it represents a link between the derivative of the generalized coordinates vector $\dot{q} = [\dot{x},\ \dot{y},\ \dot{z},\ \dot{\theta},\ \dot{\delta},\ \dot{\psi},\ \dot{\gamma}]^\top$, and the pendulum linear and angular velocity vector. In particular, the procedure detailed for a generic IRM WEC, can be sum up for the vertically-hinged pendulum through the following matrices:

- The kinematic link matrix, denoted as J_G, transforms the generalized velocity vectors $\dot{X}$ and $\dot{\Phi}$ into the pendulum-based velocity V_g and Ω_g. Specifically, Eq. (12) provides a clear definition by noting that the general rotation $\mathcal{R}_u$ corresponds to the rotation of the angle γ, about the axis $\hat{\zeta}$. Thus, J_G is defined as

$$J_G = \begin{bmatrix} R_\gamma^\top C^\top & -R_\gamma^\top \tilde{r} D \\ 0 & R_\gamma^\top D \end{bmatrix}. \tag{34}$$

- The total system velocity, expressed in the $\mathcal{R}(\mathcal{G}'\xi\eta\zeta)$ frame, can be derived recalling that the total velocity is expressed as the sum of the floater velocity and the proper velocity of the pendulum system, *i.e* via the following relation:

$$\begin{bmatrix} V_I \\ \Omega_I \end{bmatrix} = \begin{bmatrix} R_\gamma^\top C^\top & -R_\gamma^\top \tilde{r} D & 0 \\ 0 & R_\gamma^\top D & e_3^3 \end{bmatrix} \begin{bmatrix} \dot{X} \\ \dot{\Phi} \\ \dot{\gamma} \end{bmatrix}. \tag{35}$$

- Finally, the angular velocity component of the pendulum, seen as the end-effector of the kinematic chain, can be computed through the expression reported in Table 3.
- The position of the system is defined with respect to the inertial frame through the position vector $p_m \in \mathbb{R}^3$, *i.e.*

$$p_m = T^1 T^2 l_v, \tag{36}$$

where $l_v = [\ l_p\ 0\ 0\ ]^\top$ is the position of the pendulum mass with respect to its rotation axis and the roto-translation matrices T^1 and T^2 are

$$T^1 = \begin{bmatrix} C & \begin{bmatrix} x \\ y \\ z \end{bmatrix} \\ 0 & 1 \end{bmatrix}, T^2 = \begin{bmatrix} R_\gamma & \begin{bmatrix} x_0 \\ y_0 \\ z_0 \end{bmatrix} \\ 0 & 1 \end{bmatrix}. \tag{37}$$

5.2. Vertically-hinged pendulum: Dynamic equations

After the definition of the system kinematics, the kinetic energy of the system under analysis can be derived through the application of the kinetic and potential energy formulation, as described in Eqs. (56) and (57), recalling that such an IRM system is schematized exclusively through a single rigid body, *i.e.* $n = 1$, whose inertia tensor $I_p = \text{diag}(I_{xx}, I_{yy}, I_{zz})$, encloses the diagonal terms $I_{xx} \in \mathbb{R}^+$, $I_{yy} \in \mathbb{R}^+$ and $I_{zz} \in \mathbb{R}^+$. To avoid overflowing this section, Appendix C reports the explicit formulation of the energy term for the described system. However, the Lagrange equation characterizing the pendulum proper dynamics, on its related DoF is explicitly stated hereafter

$$\frac{d}{dt}\frac{\partial \mathcal{T}}{\partial \omega_\zeta} - \omega_\eta \frac{\partial \mathcal{T}}{\partial \omega_\xi} + \omega_\xi \frac{\partial \mathcal{T}}{\partial \omega_\eta} - v_\eta \frac{\partial \mathcal{T}}{\partial v_\xi} + v_\xi \frac{\partial \mathcal{T}}{\partial v_\eta} + G_{r_\zeta} = C_1. \tag{38}$$

In particular, applying the Lagrange equation, in matrix form, for the 6 DoF, the whole IRM dynamics can be computed on the $\mathcal{R}(\mathcal{G}\xi\eta\zeta)$ reference frame, whose complete expression is stated as follows

$$\begin{bmatrix} m_p & 0 & 0 & 0 & 0 & 0 \\ 0 & m_p & 0 & 0 & 0 & m_p l_p \\ 0 & 0 & m_p & 0 & -m_p l_p & 0 \\ 0 & 0 & 0 & I_\xi & 0 & 0 \\ 0 & 0 & -m_p l_p & 0 & I_\eta & 0 \\ 0 & m_p l_p & 0 & 0 & 0 & I_\zeta \end{bmatrix} \begin{bmatrix} \dot{v}_\xi \\ \dot{v}_\eta \\ \dot{v}_\zeta \\ \dot{\omega}_\xi \\ \dot{\omega}_\eta \\ \dot{\omega}_\zeta \end{bmatrix} + \begin{bmatrix} 0 & -m_p\omega_\zeta & m_p\omega_\eta & 0 & -m_p l_p \omega_\eta & -m_p l_p \omega_\zeta \\ m_p\omega_\zeta & 0 & -m_p\omega_\xi & 0 & -m_p l_p \omega_\xi & 0 \\ -m_p\omega_\eta & m_p\omega_\xi & 0 & 0 & 0 & m_p l_p \omega_\xi \\ 0 & 0 & 0 & 0 & I_\zeta \omega_\zeta & -I_\eta \omega_\eta \\ m_p l_p \omega_\eta & -m_p l_p \omega_\xi & 0 & -I_\zeta \omega_\zeta & 0 & I_\xi \omega_\xi \\ m_p l_p \omega_\zeta & 0 & -m_p l_p \omega_\xi & I_\eta \omega_\eta & -I_\xi \omega_\xi & 0 \end{bmatrix} \begin{bmatrix} v_\xi \\ v_\eta \\ v_\zeta \\ \omega_\xi \\ \omega_\eta \\ \omega_\zeta \end{bmatrix} + J_G^{-\top} \begin{bmatrix} \frac{\partial \mathcal{U}^*}{\partial x} \\ \frac{\partial \mathcal{U}^*}{\partial y} \\ \frac{\partial \mathcal{U}^*}{\partial z} \\ \frac{\partial \mathcal{U}^*}{\partial \theta} \\ \frac{\partial \mathcal{U}^*}{\partial \delta} \\ \frac{\partial \mathcal{U}^*}{\partial \psi} \end{bmatrix} = \begin{bmatrix} F_\xi \\ F_\eta \\ F_\zeta \\ T_\xi \\ T_\eta \\ T_\zeta \end{bmatrix}. \tag{39}$$

Note that m_p is the total mass of the pendulum, while the inertia terms $\{I_\xi, I_\eta, I_\zeta\} \subset \mathbb{R}^{3\times3}$ are defined as

$$I_\xi = I_{xx}\ , \quad I_\eta = I_{yy} + m_p l_p^2\ , \quad I_\zeta = I_{zz} + m_p l_p^2. \tag{40}$$

Eq. (39) displays the set of equations related to the reacting mass. Notably, the vertically-hinged pendulum is free to rotate about the vertical axis, which is defined by the versor $\hat{\zeta}$. Consequently, the sixth row of the proposed equation specifies the set of parametric forcing functions activating the pendulum, hereafter stated:

$$(I_{zz} + m_p l_p^2)\dot{\omega}_\zeta + m_p l_p \dot{v}_\eta + (I_{yy} - I_{xx})\omega_\eta \omega_\xi - m_p l_p v_\zeta \omega_\xi + m_p l_p v_\xi \omega_\eta + G_{r_\zeta} = f_{pto}. \tag{41}$$

The remaining equations represent the forces generated by the pendulum that are exerted on the floater, to which it is constrained. Such a reaction forces, are computed on the IRM frame, hence further transformation are required to define them on the floater frame, or inertial frame, according to the requirement, as shown in Section 4.2. Appendix C computes in detail the potential energy of the system, highlighting that the gravity effect generates a coupling of the system with the roll and pitch DoF, *i.e.* $G_{r_\zeta} = m_p g(l_p s_\delta s_\gamma + l_p c_\delta s_\theta c_\gamma)$. However, the couplings will be further emphasized in a subsequent section through the linear representation of the system.

5.3. Vertically-hinged pendulum: Linearized dynamics

This section aims to simplify Eq. (39), and to express the reaction forces as a function of the generalized coordinate vector q. For this purpose we adopt the assumption of small roll θ, pitch δ, and yaw ψ

$$\bar{M} = \begin{bmatrix} m_p & 0 & 0 & 0 & m_p z_0 & -m_p y_0 & 0 \\ 0 & m_p & 0 & -m_p z_0 & 0 & m_p(x_0 + l_p) & m_p l_p \\ 0 & 0 & m_p & m_p y_0 & -m_p(x_0 + l) & 0 & 0 \\ 0 & -m_p z_0 & m_p y_0 & I_{xx} + m_p(y_0 + z_0)^2 & -m_p y_0(x_0 + l_p) & -m_p z_0(x_0 + l_p) & -m_p l_p z_0 \\ m_p z_0 & 0 & -m_p x_0 & m_p x_0 y_0 & I_{yy} + mpz_0^2 + m_p(l_p - x_0)^2 & -m_p z_0 y_0 & 0 \\ -m_p y_0 & m_p(x_0 + l_p) & 0 & -m_p(x_0 + l_p) z_0 & -m_p y_0 z_0 & I_{zz} + m_p y_0^2 + m_p(x_0 + l_p)^2 & I_{zz} + m_p l_p^2 + m_p l_p x_0 \\ 0 & m_p l_p & 0 & -m_p l_p z_0 & 0 & I_{zz} + m_p l_p^2 + m_p l_p x_0 & I_{zz} + m_p l_p^2 \end{bmatrix},$$

$$\bar{K} = \begin{bmatrix} 0 & 0 & 0 & 0 & 0 & 0 & 0 \\ 0 & 0 & 0 & 0 & 0 & 0 & 0 \\ 0 & 0 & 0 & 0 & 0 & 0 & 0 \\ 0 & 0 & 0 & -m_p g z_0 & 0 & 0 & m_p l_p g \\ 0 & 0 & 0 & 0 & -m_p g z_0 & 0 & 0 \\ 0 & 0 & 0 & 0 & 0 & 0 & 0 \\ 0 & 0 & 0 & m_p l_p g & 0 & 0 & m_p l_p g \end{bmatrix}, \tag{42}$$

Box I.

rotation and we consider that the dynamics of the pendulum is close to the zero equilibrium, implying that the system dynamics, in linearized form, can be expressed through two different matrices, stated as (see Box I).

where $\bar{M} \in \mathbb{R}^{7\times7}$ and $\bar{K} \in \mathbb{R}^{7\times7}$ are the linearized mass and stiffness matrices, respectively. Note that no damping matrix results from linearization. The reader can refer to the Appendix C for further details on the overall linearization procedure. The linear representation effectively demonstrates how the main floater modes are coupled with the IRM. The primary effects arise from stiffness coupling which links floater's roll motion with the pendulum rotation angle. Moreover, the pendulum couples in terms of mass with the sway, heave, and yaw DoF, noting that the latter DoF is parallel to the pendulum's axis of rotation. In particular, the reaction force expression and the system mass matrices, expressed in nonlinear form in Eq. (43), can be stated, after the linearization procedure, as follows:

$$\begin{bmatrix} f_{bk} \\ C_1 \end{bmatrix} = \bar{K} q, \qquad \begin{bmatrix} M_m & I_{mf} \\ I_{fm} & I_m \end{bmatrix} = \bar{M}. \tag{43}$$

5.4. Generalization of the IRM equation of motion

The motion of the floater represents a parametric excitation for this family of devices. For this purpose, Table 4 displays the equations of motion that characterize the dynamics of the reacting mass. Specifically, for each system considered, the nonlinear equation is presented along with its linearized version. Notably, several adjustments can be made in cases involving gyroscopic effects and the horizontal pendulum. Gyroscopes, both vertical and perpendicular, can stall if the time-varying polar axis of the flywheel becomes parallel to the floater's rotation axis. This issue is addressed in the literature by adding a recall mass [83] or unbalancing the gimbal, which introduces stiffness to the system and alters the equilibrium point. Meanwhile, the vertical pendulum stalls if the arm vector r_{m_v} becomes perpendicular to the floater's rotation axis. This problem is typically resolved by designing floaters that can pitch and roll simultaneously, such as the unbalanced floater in the case of the Penguin device [22]. Note that for the gimbaled pendulum, three equations are introduced because they are expressed in relation to the frame associated with the last joint, within the $\mathcal{R}_{\xi\eta\zeta}$ frame. Specifically, β is obtained by integrating the second equation with respect to $\omega_\eta = V_{I_2} + \dot{\beta}$. To determine α, both the first and third equations are required, where $\omega_\xi = V_{I_1} + \cos\beta\dot{\alpha}$ and $\omega_\zeta = V_{I_3} + \sin\beta\dot{\alpha}$.

For each device, under the assumption of small rotations, the corresponding linear equations are presented. Specifically, the linear representation of the system provides an initial insight into the system dynamics, highlighting the primary coupling between the floater and the considered IRM, which are reported in Table 5. It emphasizes that the pendulum and sliding mass introduce inertial and elastic interaction, while gyroscopic systems exhibit Coriolis-like coupling, which is proportional to the spinning velocity of the flywheel $\dot{\varphi}$. Note that each system introduces a coupling where rotational and linear interactions coexist within the same plane. However, the gimbaled pendulum, because of its nature, is activated regardless of the floater's motion. Note that the sliding mass introduces a static effect due to the weight of the mass, which does not need to be considered in dynamic analysis since it can be treated as statically balanced.

6. A comparison with a benchmark numerical solver

Following the procedure discussed in the previous section, including the computations performed in the Appendix C, we compare the analytical model derived using the proposed methodology, with a numerical solution computed using Simscape multi-body, which is part of the Matlab Simulink suite. In particular, the output of such considered approaches are compared, to showcase a numerical validation of the general modeling procedure proposed in this paper. Therefore, Section 6.1 introduces the comparison of output signals between the analytical model and the commercial software Simscape, while Section 6.2 presents an additional methodology for computing the load on supporting mechanical components such as the bearings.

6.1. Results

As a case study, we select a hinged vertical pendulum, which has been modeled through a very basic geometry, based on a parallelepiped solid, with its main dimensions being the length a, the width b, and the height h. The selected pendulum mass is 65 tons, considering a concrete solid material, whose main inertia value are reported in Table 6. Simscape enables the rapid modeling of physical systems within the Simulink environment by connecting block diagrams and integrating various modeling paradigms, making it easier to simulate complex, real-world behaviors. In this environment, kinematic transformations, are implemented through a structured scheme, generating an intuitive dynamic representation of the system. A possible base diagram to model such a system is reported in Fig. 6, whose main characteristics are hereafter introduced: The light orange diagram illustrates the transformation between reference frames, as specified in Section 3.1. Specifically, the first two blocks on the left of the figure replicate the

Table 4
Equation of motion related to the reacting mass dynamics.

IRM type	Tipology	Dynamic equation
Pendulum	Vertical axis	$(I_{zz}+m_pl_p^2)\dot{\omega}_\zeta+m_pl_p\dot{v}_\eta+(I_{yy}-I_{xx})\omega_\eta\omega_\xi-m_pl_pv_\zeta\omega_\xi+m_pl_pv_\xi\omega_\eta+G_{r_\zeta}=C_1$ $m_pl_p\ddot{y}-m_pl_pz_0\ddot{\theta}+(I_{zz}+m_pl_p^2+m_pl_px_0)\ddot{\psi}+(I_{zz}+m_pl_p^2)\ddot{\gamma}+m_pl_pg\theta+m_pl_pg\gamma=C_1$
	Horizontal axis	$(I_{xx}+m_pl_p^2)\dot{\omega}_\xi+m_pl_p\dot{v}_\eta+(I_{zz}-I_{yy}-m_pl_p^2)\omega_\eta\omega_\zeta+m_pl_pv_\xi\omega_\zeta-m_pl_pv_\zeta\omega_\xi+G_{r_\xi}=C_1$ $m_pl_p\ddot{y}+(I_{xx}+m_pl_p^2-m_pl_pz_0)\ddot{\theta}+m_pl_px_0\ddot{\psi}+(I_{xx}+m_pl_p^2)\ddot{\alpha}+m_pl_pg\theta+m_pl_pg\alpha=C_1$
	Gimbaled	$(I_{xx}+m_pl_p^2)\dot{\omega}_\xi+m_pl_p\dot{v}_\eta+(I_{zz}-I_{yy}-m_pl_p^2)\omega_\eta\omega_\zeta+m_pl_pv_\xi\omega_\zeta-m_pl_pv_\zeta\omega_\xi+G_{r_\xi}=C_{1,\alpha}\cos\beta$ $(I_{yy}+m_pl_p^2)\dot{\omega}_\eta-m_pl_p\dot{v}_\xi+(I_{xx}+m_pl_p^2-I_{zz})\omega_\xi\omega_\zeta+m_pl_pv_\eta\omega_\zeta-m_pl_pv_\zeta\omega_\eta+G_{r_\eta}=C_{1,\beta}$ $I_{zz}\dot{\omega}_\zeta+(I_{yy}-I_{xx})\omega_\xi\omega_\eta+G_{r_\zeta}=C_{1,\alpha}\sin\beta$ $m_pl_p\ddot{y}+(I_{xx}+m_pl_p^2-m_pl_pz_0)\ddot{\theta}+m_pl_px_0\ddot{\psi}+(I_{xx}+m_pl_p^2)\ddot{\alpha}+m_pl_pg\theta+m_pl_pg\alpha=C_{1,\alpha}$ $-m_pl_p\ddot{x}+(I_{xx}+m_pl_p^2-m_pl_pz_0)\ddot{\delta}+m_pl_pg_0\ddot{\psi}+(I_{xx}+m_pl_p^2)\ddot{\beta}+m_pl_pg\delta+m_pl_pg\beta=C_{1,\beta}$
Gyroscope	Vertical axis	$I_{zz}\dot{\omega}_\zeta+(I_{yy}-I_{xx})\omega_\xi\omega_\eta-I_{xx}\omega_\eta\dot{\varphi}=C_1$ $I_{zz}\ddot{\gamma}+I_{zz}\ddot{\psi}+I_{yy}\dot{\delta}\dot{\varphi}=C_1$
	Horizontal axis	$I_{xx}\dot{\omega}_\xi+(I_{zz}-I_{yy})\omega_\zeta\omega_\eta+I_{zz}\omega_\eta\dot{\varphi}=C_1$ $I_{xx}\ddot{\alpha}+I_{xx}\ddot{\theta}+I_{zz}\dot{\delta}\dot{\varphi}=C_1$
Sliding mass	Vertical axis	$m_s\dot{v}_\zeta-m_s\omega_\eta v_\xi-m_s\omega_\eta^2\gamma+m_s\omega_\xi v_\eta-m_s\omega_\xi^2\gamma+G_{l,\zeta}=C_1$ $m_s\ddot{z}+m_s\ddot{\gamma}+m_sg=C_1$
	Horizontal axis	$m_s\dot{v}_\xi-m_s\omega_\zeta v_\eta-m_s\omega_\xi^2\alpha+m_s\omega_\eta v_\zeta-m_s\omega_\eta^2\alpha+G_{l,\xi}=C_1$ $m_s\ddot{x}+m_s\ddot{\alpha}-m_sg\delta=C_1$

Table 5
Visualization of the floater DoF coupled with the reacting mass.

IRM type	Tipology	Inertial						Coriolis						Stiffness					
		S	Sw	H	R	P	Y	S	Sw	H	R	P	Y	S	Sw	H	R	P	Y
Pendulum	Vertical axis		■		■		■										■		
	Horizontal axis		■		■		■										■		
	Gimbaled	■	■		■	■											■	■	
Gyroscope	Vertical axis						■					■							
	Horizontal axis				■							■							
Sliding mass	Vertical axis			■														■	
	Horizontal axis	■																■	

transformation from $\mathcal{R}(OXYZ) \mapsto \mathcal{R}(\mathcal{O}'xyz)$, while the hinge block on the right represents the projection of the kinematics onto $\mathcal{R}(\mathcal{G}\xi\eta\zeta)$, through the angle γ. The gray 'Rigid transform' block facilitates the mapping of kinematics from $\mathcal{R}(\mathcal{O}'xyz)$ to $\mathcal{R}(\mathcal{G}\Xi\mathcal{H}\mathcal{Z})$, taking into account the r vector, which expresses the position of the second frame with respect to the first one. The body blocks represent a fictitious hull, included for visualization purposes exclusively, considering that the system kinematics is posed through the p vector. On the other hand, the pendulum mass blocks encapsulate all the inertial properties of the IRM system. Note that the green tag highlights the measured system output, encompassing the pendulum rotation angle γ, the reaction forces f_{rc} acting on the inertial frame, and the vector of reaction forces acting on the shaft. The nature and significance of the latter forces are discussed in Section 6.2.

Inputs are simple sinusoidal functions, that mimic a prescribed floater motion obtained through a regular wave condition [62]. In particular, the input function $f(t) \in \mathbb{R}$, $t \mapsto f(t)$ has the following prescribed form

$$f(t) = A_0 \sin(\omega_0 t), \tag{44}$$

where $\omega_0 = 2\pi/T_0$, with $T_0 = 5$ s, that is the most representative period of the Mediterranean Sea [84], and the amplitude A_0 is set equal to 1 m, for the linear DoFs, and 20° for the rotating ones. We simulate the analytical equations using the Runge–Kutta method [85]

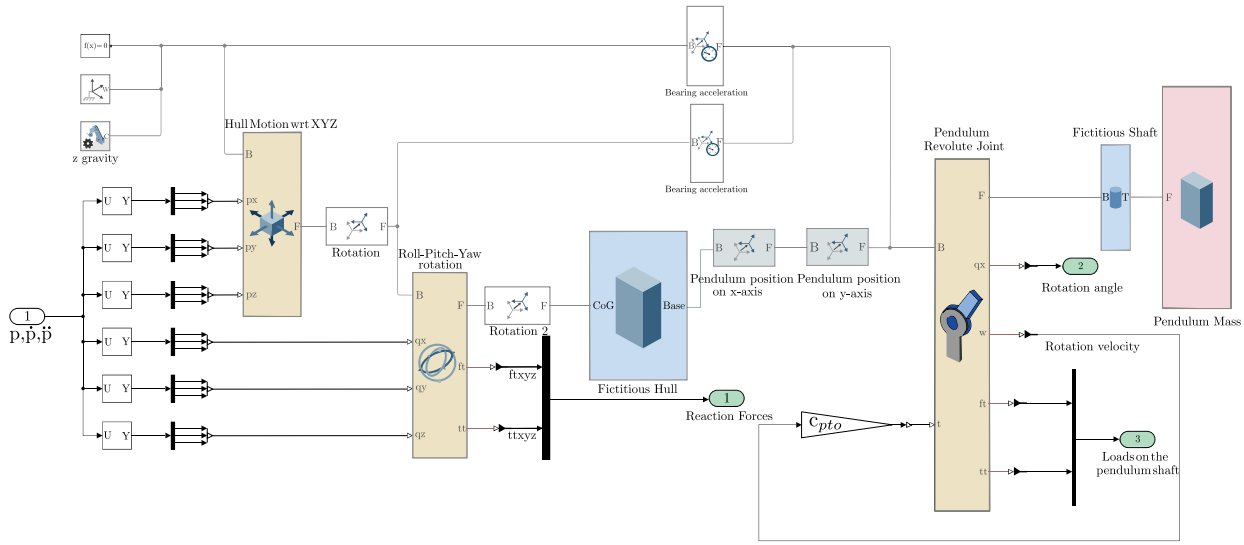

Fig. 6. Block diagram representation in the Simscape environment. Each block color represents a specific meaning: orange blocks denote the joints, including the floater-associated joint and the mechanism-related joint. The blue blocks represent fictitious bodies, inserted exclusively for visualization purposes. The pink block signifies the pendulum mass, encompassing its mass and inertia.

in the MATLAB-Simulink environment with the *ode4* function, applying a fixed step size of 0.01 s.

The resolution procedure is summarized in the Algorithm 1, where every calculation step, executed by the solver, is detailed, *i.e.* the kinematic definition, the solution for the pendulum rotation, that with its first and second derivatives, define the forces acting on the floater.

Algorithm 1 Algorithm for dynamic interactions computation

Require: $p[n] : \forall n \in \mathbb{N}$,
Set the pendulum initial position and velocity ($\gamma[0]$, $\gamma[1]$)
for k = 2, k $\leq T_{sim}/\Delta t, k++$ **do**
$[V_I[k-1]\ \Omega_I[k-1]] \leftarrow$ (35) ▷ System velocity vector
$[V_I[k]\ \Omega_I[k]] \leftarrow$ (63) ▷ System acceleration vector
$\gamma(k) \leftarrow$ (41) ▷ Pendulum angular acceleration
$M_I[k],\ B_I[k],\ K_I[k] \leftarrow$ (39) ▷ Coupling matrices in the pendulum space
$M_i[k],\ B_i[k],\ K_i[k] \leftarrow$ (30) ▷ Coupling matrices in the inertial space
$f_{rc_m} \leftarrow$ (31) ▷ Reaction forces
end for

Note that the reaction force here incorporates inertial effects, Coriolis and centrifugal forces, and action due to the gravity. Nevertheless, for a further simulation of a WEC system, the inertial terms have to be separated and to be added to the floater inertia matrix to solve the differential equation, avoiding any potential algebraic loop. Moreover, the pendulum control torque is parameterized through the damping parameter $c_{pto} \in \mathbb{R}^+$, which is designed leveraging the so-called impedance-matching conditions [10,86].

In Fig. 7, we observe a comparison of the pendulum rotation γ, demonstrating a precise match over the simulated 300 s. A zoom in the last 100 s of simulation showcases the alignment between the proposed analytical framework and the Simscape simulation, accounting for both transient and steady-state conditions. Moving to Fig. 8, which presents the load feedback to the floater, indistinguishable responses can be appreciated, further validating the proposed analytical framework.

For sake of completeness, Fig. 7 represents the instantaneous absorbed mechanical power $P_a \in \mathbb{R}^+, t \mapsto P_a$, computed as follows:

$$P_a = C_1\dot{\gamma} \implies P_a = c_{pto}\dot{\gamma}^2. \tag{45}$$

Table 6
Case study: pendulum main properties.

Name	Symbol	Value	Unit
Pendulum mass	m_p	65×10^3	kg
Pendulum arm	l_p	1.5	m
Pendulum mass length	a	3	m
Pendulum mass width	b	2	m
Pendulum mass height	h	5	m
Pendulum inertia wrt x-axis	I_{xx}	1.5708×10^5	kgm^2
Pendulum inertia wrt y-axis	I_{yy}	1.8417×10^5	kgm^2
Pendulum inertia wrt z-axis	I_{zz}	7.0417×10^4	kgm^2
Pendulum shaft position on wrt x-axis	x_0	2	m
Pendulum shaft position on wrt y-axis	y_0	2	m
Pendulum shaft position on wrt z-axis	z_0	0	m
Control damping	c_{pto}	5×10^5	Nms/rad

recalling that the control action is $C_1 = c_{pto}\dot{\gamma}$. Note that the Appendix D provides an explicit expression for the reaction force vector and pendulum angle, considering the associated floater input, generated by an irregular wave simulation.

6.2. Bearings loads computation

The proposed method for computing dynamic couplings can be applied to perform an analysis on the loads on the rotating shaft of the pendulum. This information is crucial for sizing mechanical components, *e.g.* the bearings linking the shaft to the floater frame. These play a crucial role in supporting the pendulum and absorbing the radial load resulting from the coupling between the IRM and the floater. Typically, when a vertical rotating shaft is involved, an axial bearing is chosen to bear the axial load, while a pair of radial bearings is selected to handle the radial load. Firstly, it is relevant to project the loads computed through Eq. (27) into the $R(\mathcal{G}\Xi\mathcal{H}\mathcal{Z})$ frame, and the following relation

$$\bar{R}_\gamma M_I J_I \ddot{q} + \bar{R}_\gamma M_I \dot{J}_I \dot{q} + \bar{R}_\gamma B_I J_I \dot{q} + J_M^{-\mathsf{T}} G(q) = f_{rc_{\Xi\mathcal{H}\mathcal{Z}}}. \tag{46}$$

holds, where $f_{rc_{\Xi\mathcal{H}\mathcal{Z}}} = [F_\Xi\ F_\mathcal{H}\ F_\mathcal{Z}\ T_\Xi\ T_\mathcal{H}\ T_\mathcal{Z}]^\mathsf{T}$, and $F_\Xi \in \mathbb{R}$, $F_\mathcal{H} \in \mathbb{R}$, $F_\mathcal{Z} \in \mathbb{R}$, $T_\Xi \in \mathbb{R}$, $T_\mathcal{H} \in \mathbb{R}$ and $T_\mathcal{Z} \in \mathbb{R}$ are the reaction forces acting along the pendulum rotating shaft. Moreover, the rotation matrix $\bar{R}_\epsilon$ to project the reaction forces from $R(\mathcal{G}\xi\eta\zeta)$ to $R(\mathcal{G}\Xi\mathcal{H}\mathcal{Z})$ can explicitly expressed as follows:

$$\bar{R}_\gamma = \begin{bmatrix} R_\gamma & 0 \\ 0 & R_\gamma \end{bmatrix}. \tag{47}$$

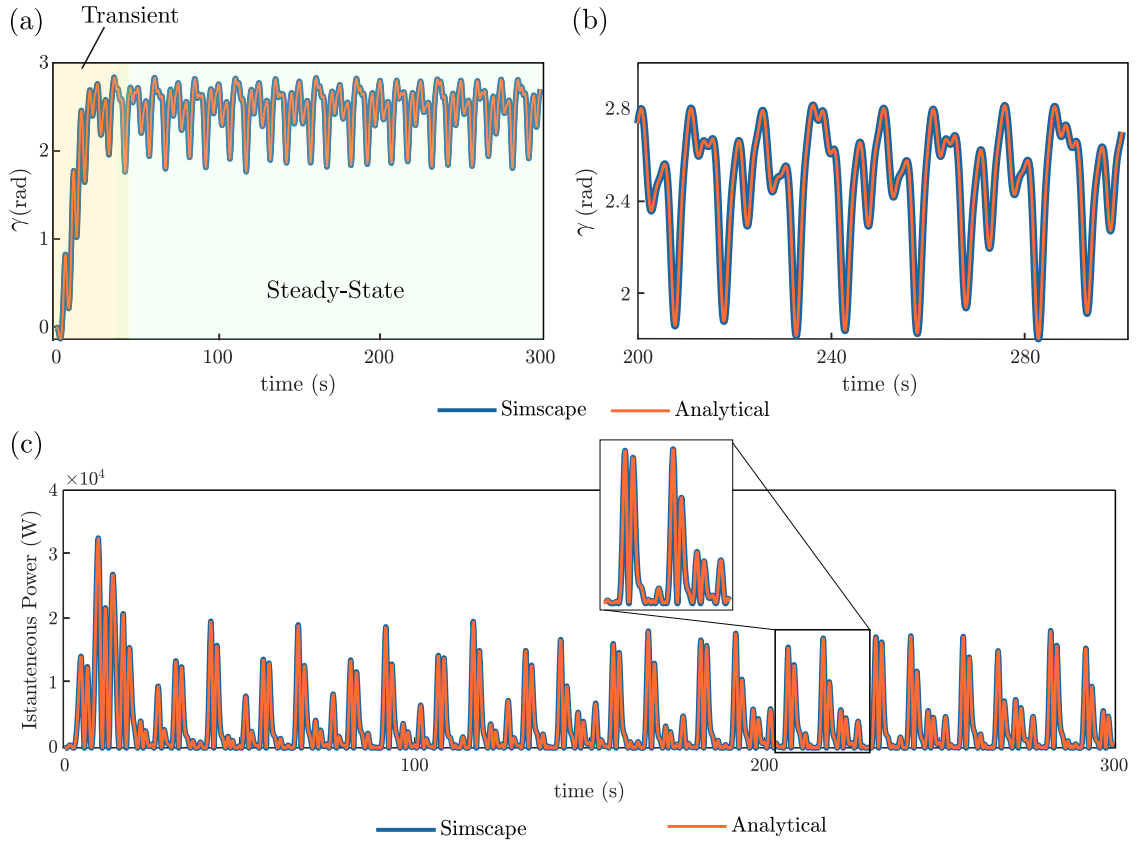

Fig. 7. Comparison of signals between the analytical model and the Simscape model, simulating a regular wave. (a) Pendulum rotation angle for the entire simulation duration of 300 s. (b) Zoomed-in view of the pendulum rotation between 200 s and 300 s. (c) Power production considering a predefined damping factor c_{pto} for both modeling approaches, with a zoom-in on a specific signal window.

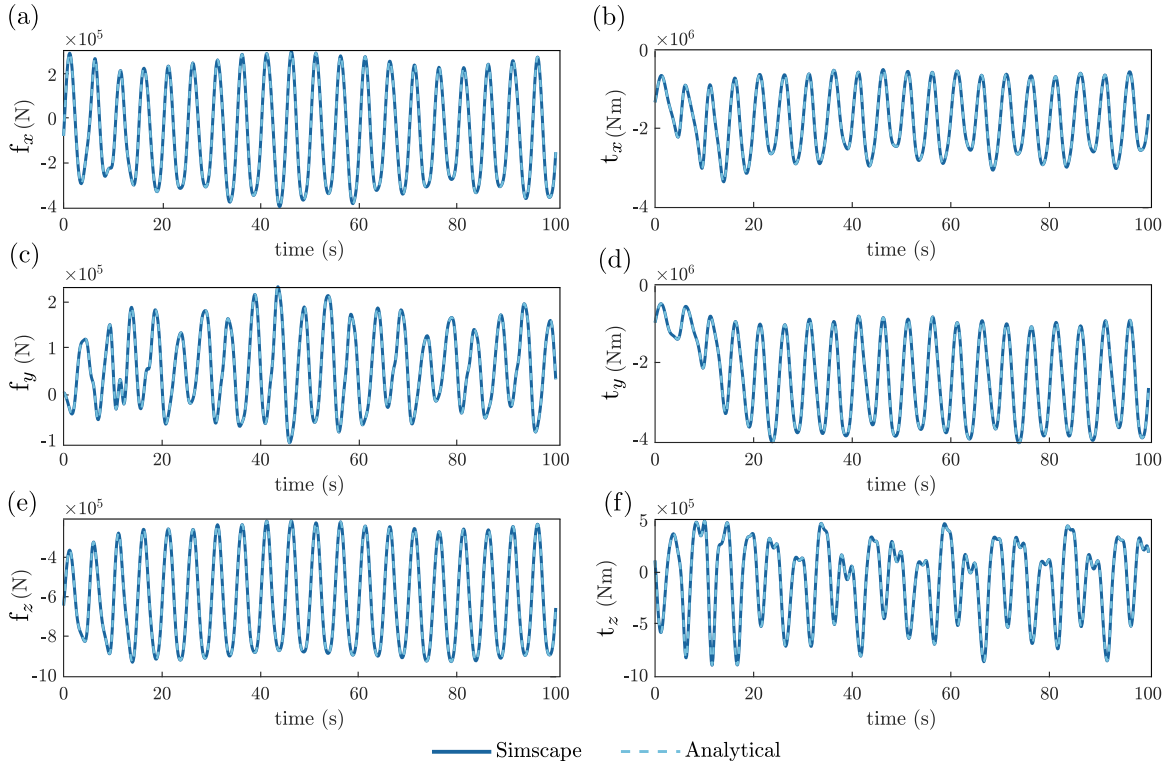

Fig. 8. Reaction forces acting on the floater through the pendulum constraints: comparison between the analytical model and the Simscape model, simulating a regular wave signal. The panel figure shows (a) the reaction force acting on the x-axis, (b) the reaction torque acting on the x-axis, (c) the reaction force acting on the y-axis, (d) the reaction torque acting on the y-axis, (e) the reaction force acting on the z-axis, and (f) the reaction torque acting on the z-axis.

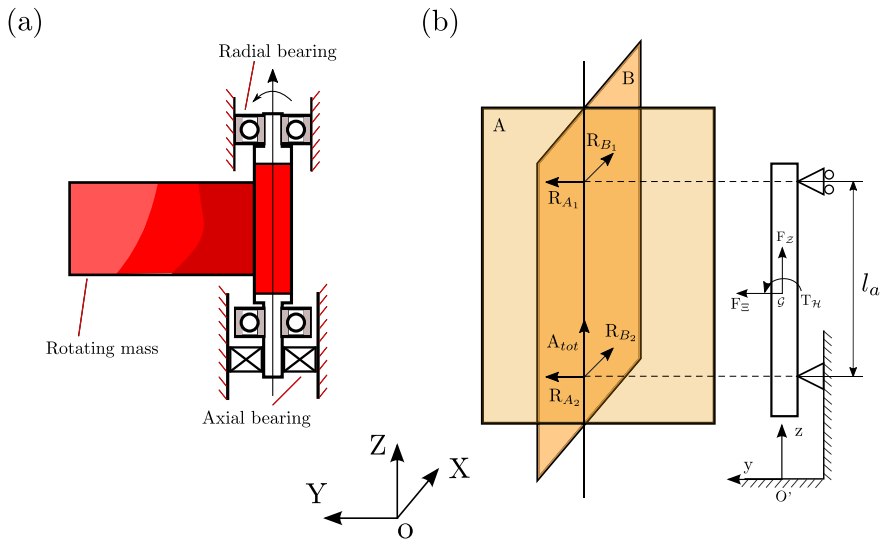

Fig. 9. Schematic representation of a possible bearing configuration. (a) Bearing configuration with a pair of radial bearings and an axial bearing. (b) Related scheme for load computation, considering the shaft as a supported beam on two perpendicular planes, A and B. *A* and *B*.

The proposed configuration is represented in terms of a schematic diagram in Fig. 9. The computation of the overall load acting on the bearings can be decomposed into two different planes, *A* and *B*, that allows to model the bearing configuration in terms of a fixed and a hinged support, with the former constraining the system over the axial loads. In particular, knowing that l_s is the inter-axial distance between the two radial bearings, the constraints forces $R_{A_1} \in \mathbb{R}$ and $R_{A_2} \in \mathbb{R}$, acting over the radial direction on the *A* plane, are computed solving the beam element, and hence the following relation

$$R_{A_1} = \frac{F_\Xi}{2} - \frac{T_\mathcal{H}}{l_s}, \qquad R_{A_2} = \frac{F_\Xi}{2} + \frac{T_\mathcal{H}}{l_s}, \tag{48}$$

holds, while the constraints forces $R_{B_1} \in \mathbb{R}$ and $R_{B_2} \in \mathbb{R}$, acting over the radial direction on the *B* plane, can be computed as follows:

$$R_{B_1} = \frac{F_\mathcal{H}}{2} - \frac{T_\Xi}{l_s}, \qquad R_{B_2} = \frac{F_\mathcal{H}}{2} + \frac{T_\Xi}{l_s}. \tag{49}$$

Finally the total radial force acting on each bearings $R_{bear_1} \in \mathbb{R}^+$ and $R_{bear_1} \in \mathbb{R}^+$ is obtained summing the two components in terms of the following relation:

$$R_{bear_1} = \sqrt{R_{A_1}^2 + R_{B_1}^2}, \qquad R_{bear_2} = \sqrt{R_{A_2}^2 + R_{B_2}^2}, \tag{50}$$

where R_{bear_1} and R_{bear_2} are the radial loads required for a suitable selection of bearings for such an application. The computation of the axial load $A_{tot} \in \mathbb{R}$ for sizing the radial bearings is then straightforward, noting that it corresponds directly to the force $F_\mathcal{Z}$, *i.e.* $A_{tot} = F_\mathcal{Z}$.

7. Conclusions

This paper presents a comprehensive framework for modeling the mechanical interactions of IRM WECs. It emphasizes a versatile modeling scheme applicable across a broad spectrum of IRM WECs. The methodology is detailed through a step-by-step procedure, covering the derivation of the reacting system's dynamic equations and the characterization of the reaction forces exerted by the reacting system on the floater. This comprehensive mechanical model is valuable for WEC simulation, taking into account 6 DoF.

The analytical model provides distinct advantages for a deep understanding of physical interactions and facilitates the formulation of a modeling approach tailored for control applications. Due to its analytical nature, the model can be readily linearized, allowing the application of established linear control strategies.

This approach, in particular, highlights the strongest modes of motion involved in the interactions between the floater and the internal reacting system. Specifically, it has been observed that the pendulum and sliding system primarily introduce inertial and elastic coupling. In contrast, for technologies relying on the gyroscopic system the Coriolis coupling, due to the interaction between the flywheel's angular momentum and the floater's rotational velocity, is the most relevant effect.

Furthermore, to illustrate the applicability of this framework, we conduct a case study, choosing a mechanism commonly employed in the WEC literature for harnessing energy, *i.e.* the vertically-hinged pendulum. By comparing the time series of resulting reaction forces F_{rc}, and the rotation angle γ with the simulation tool Matlab Simscape, we verify the consistency of our proposed approach, showing a perfect match against this well-established numerical solver.

CRediT authorship contribution statement

Fabio Carapellese: Writing – original draft, Software, Methodology, Investigation, Data curation, Conceptualization. **Nicolás Faedo:** Writing – review & editing, Supervision, Resources, Investigation.

Declaration of competing interest

The authors declare that they have no known competing financial interests or personal relationships that could have appeared to influence the work reported in this paper.

Data availability

Data will be made available on request.

Acknowledgments

Project funded by the European Union – NextGenerationEU Award Number: Project code PE0000021, Concession Decree No. 1561 of 11.10.2022 adopted by Ministero dell'Universitá e della Ricerca (MUR), Italy, CUP, Italy E13C22001890001, Project title "Network 4 Energy Sustainable Transition – NEST".

Appendix A

The Euler equation for a body moving in 6 DoF is expressed as follows

$$\begin{aligned} &m_f\dot{v}_x + m_f\omega_y v_z - m_f\omega_z v_y = F_x,\\ &m_f\dot{v}_y + m_f\omega_z v_x - m_f\omega_x v_z = F_y,\\ &m_f\dot{v}_z + m_f\omega_x v_y - m_f\omega_y v_x = F_z,\\ &I_x\dot{\omega}_x + \omega_y\omega_z(I_z - I_y) = M_x,\\ &I_y\dot{\omega}_y + \omega_x\omega_z(I_x - I_z) = M_y,\\ &I_z\dot{\omega}_z + \omega_x\omega_y(I_y - I_x) = M_z, \end{aligned} \tag{51}$$

where $F_{ext} = [F_x\ F_y\ F_z\ M_x\ M_y\ M_z]^\top \in \mathbb{R}^6$ is the vector of external forces in the body-fixed frame. In matrix form, Eq. (51) can be rewritten as follows:

$$M_F\dot{w}_{xyz} + B_F(w_{xyz})w_{xyz} = F_{ext}, \tag{52}$$

with the matrices M_F and B_F explicitly computed as

$$M_F = \begin{bmatrix} m_f & 0 & 0 & 0 & 0 & 0\\ 0 & m_f & 0 & 0 & 0 & 0\\ 0 & 0 & m_f & 0 & 0 & 0\\ 0 & 0 & 0 & I_x & 0 & 0\\ 0 & 0 & 0 & 0 & I_y & 0\\ 0 & 0 & 0 & 0 & 0 & I_z \end{bmatrix},$$

$$B_F = \begin{bmatrix} 0 & -m_f\omega_z & m_f\omega_y & 0 & 0 & 0\\ m_f\omega_z & 0 & -m_f\omega_x & 0 & 0 & 0\\ -m_f\omega_y & m_f\omega_x & 0 & 0 & 0 & 0\\ 0 & 0 & 0 & 0 & I_z\omega_z & -I_y\omega_y\\ 0 & 0 & 0 & -I_z\omega_z & 0 & I_x\omega_x\\ 0 & 0 & 0 & I_y\omega_y & -I_x\omega_x & 0 \end{bmatrix}. \tag{53}$$

Appendix B

This appendix explores kinematic relations and concepts fundamental for analyzing the kinematics of IRM WECs. Initially, we introduce the concept of quasi-coordinates. If $q(t)$ is the vector of generalized coordinates, and $q_k(t)$ are its components, referred as *true-coordinates*. This terminology implies that if the $\dot{q}_k(t)$ is a known function of time, integrating it with respect to time, yields the corresponding vector component $q_k(t)$. However, it is also feasible to establish a set of differential equations that do not solely rely on true coordinates. A vector ω_s can be defined as a linear combination of n independent velocity vector component $\dot{q}_k$. Fr such a case the variables ω_s cannot be integrated to obtain the true coordinates $\dot{q}_k$. These variables, called *quasi-coordinates* are expressed in the form

$$\omega_s = \alpha_{s1}\dot{q}_1 + \alpha_{s2}\dot{q}_2 + \cdots + \alpha_{sn}\dot{q}_2, \tag{54}$$

where the coefficients α_{sr}, $r \in \mathbb{N}_n$, are known functions of the generalized coordinates component q_k. The Lagrange equations for quasi-coordinates are expressed, in matrix form, as follows:

$$\begin{aligned} &\frac{d}{dt}\left(\frac{\partial\mathcal{T}}{\partial V_I}\right) + \tilde{\Omega}_I\frac{\partial\mathcal{T}}{\partial V_I} + j_{1,1}^\top\frac{\partial\mathcal{U}}{\partial X} + j_{2,1}^\top\frac{\partial\mathcal{U}}{\partial\Phi} = F_g,\\ &\frac{d}{dt}\left(\frac{\partial\mathcal{T}}{\partial\Omega_I}\right) + \tilde{\Omega}_I\frac{\partial\mathcal{T}}{\partial\Omega_I} + \tilde{V}_I\frac{\partial\mathcal{T}}{\partial V_I} + j_{1,2}^\top\frac{\partial\mathcal{U}}{\partial X} + j_{2,2}^\top\frac{\partial\mathcal{U}}{\partial\Phi} = T_g, \end{aligned} \tag{55}$$

where $j_{1,1}$, $j_{1,2}$, $j_{2,1}$, $j_{2,2}$ are the block matrices of the inverse of the kinematic link matrix defined in Eq. (12), *i.e.* $J_G^{-1} = \begin{bmatrix} j_{1,1} & j_{1,2}\\ j_{2,1} & j_{2,2}\end{bmatrix}$. Furthermore $\mathcal{T}(V_g, \Omega_g) \in \mathbb{R}$ and $\mathcal{U}(q) \in \mathbb{R}$ represent the kinetic and potential energy of the system, respectively. These are defined for every discrete body within the mechanical system. In particular, the expression for the kinetic energy is the following:

$$\mathcal{T} = \sum_{i=1}^{n}\frac{1}{2}\Omega_{EF_i}^\top I_{m_i}\Omega_{EF_i} + \sum_{i=1}^{n}\frac{1}{2}V_{EF_i}^\top(m_{m_i}\mathbb{I}_3)V_{EF_i}, \tag{56}$$

where $m_m \in \mathbb{R}^+$ and $I_m \in \mathbb{R}^{3\times3}$ are the mass (scalar) and the inertia tensor referred to the IRM CoG, respectively. Moreover, n represents the number of discrete masses, on which the reacting system is decomposed into. Furthermore, the expression for the potential energy is the following:

$$\mathcal{U} = -\sum_{i=1}^{n} m_{m_i} g_0^\top p_{m_i}, \tag{57}$$

where g_0 is the gravity acceleration vector in the base frame, *e.g.* $g_0 = [0\ 0\ -g]^\top$, and p_{m_i} is a function only of the joint variable itself, and not of the joint velocity $\dot{q}$.

Additionally, the development of dynamic equations for IRM WECs necessitates the computation of the derivative of the Jacobian matrix. In particular, the derivative of the matrices $C^\top$ and D, are respectively:

$$\dot{C}^\top = -R_\theta^\top\tilde{\omega}_\theta R_\delta^\top R_\psi^\top - R_\theta^\top R_\delta^\top\tilde{\omega}_\delta R_\psi^\top - R_\theta^\top R_\delta^\top R_\psi^\top\tilde{\omega}_\psi, \tag{58}$$

where the matrices $\tilde{\omega}_\theta$, $\tilde{\omega}_\delta$ and $\tilde{\omega}_\psi$ are the skew-symmetric matrices defined as:

$$\omega_\theta = \begin{bmatrix} 0 & 0 & 0\\ 0 & 0 & -\dot{\theta}\\ 0 & \dot{\theta} & 0\end{bmatrix}, \omega_\delta = \begin{bmatrix} 0 & 0 & \dot{\delta}\\ 0 & 0 & 0\\ -\dot{\delta} & 0 & 0\end{bmatrix}, \omega_\psi = \begin{bmatrix} 0 & -\dot{\psi} & 0\\ \dot{\psi} & 0 & 0\\ 0 & 0 & 0\end{bmatrix}. \tag{59}$$

Further more the so called analytical Jacobian of an object rotating into space is defined by the matrix $D \in \mathbb{R}^{3\times3}$, *i.e.*

$$D = \begin{bmatrix} 1 & 0 & -s_\delta\\ 0 & c_\theta & c_\delta s_\theta\\ 0 & -s_\theta & c_\delta c_\theta\end{bmatrix}, \tag{60}$$

whose derivative is

$$\dot{D} = \begin{bmatrix} 0 & 0 & -\dot{\delta}c_\delta\\ 0 & -\dot{\theta}s_\theta & -\dot{\delta}s_\delta s_\theta + \dot{\theta}c_\delta c_\theta\\ 0 & -\dot{\theta}c_\theta & -\dot{\delta}s_\delta c_\theta - \dot{\theta}c_\delta s_\theta\end{bmatrix}. \tag{61}$$

Finally, we can compute the derivative of the Jacobian matrix J_I. Recalling that it appears as follows

$$J_I = \begin{bmatrix} R(\varepsilon,\hat{\xi})^\top C^\top & -R(\varepsilon,\hat{\xi})^\top\tilde{r}D & 0\\ 0 & R(\varepsilon,\hat{\xi})^\top D & \bar{I}\end{bmatrix}, \tag{62}$$

can be written as a general block matrix as follows

$$J_I = \begin{bmatrix} J_{I_{11}} & J_{I_{12}} & 0\\ 0 & J_{I_{22}} & \bar{I}\end{bmatrix} \implies \dot{J}_I = \begin{bmatrix} \dot{J}_{I_{11}} & \dot{J}_{I_{12}} & 0\\ 0 & \dot{J}_{I_{22}} & 0\end{bmatrix}, \tag{63}$$

where $J_{I_{11}} \in \mathbb{R}^{3\times3}, J_{I_{12}} \in \mathbb{R}^{3\times3}$, and $J_{I_{22}} \in \mathbb{R}^{3\times3}$ are the block matrices, composing J_I and $\dot{J}_{I_{11}}$, $\dot{J}_{I_{12}}$, and $\dot{J}_{I_{22}}$ are their derivative matrices, respectively. Furthermore, the following relations hold

$$\begin{aligned} \dot{J}_{I_{11}} &= \frac{d}{dt}(R_\gamma^\top C^\top) = -R_\gamma^\top\tilde{\omega}_\varepsilon C^\top + R_\gamma^\top\dot{C}^\top,\\ \dot{J}_{I_{12}} &= \frac{d}{dt}(R_\gamma^\top\tilde{r}D) = R_\gamma^\top\tilde{\omega}_\varepsilon\tilde{r}D - R_\gamma^\top\tilde{r}\dot{D},\\ \dot{J}_{I_{22}} &= \frac{d}{dt}(R_\gamma^\top D) = -R_\gamma^\top\tilde{\omega}_\gamma D + R_\gamma^\top D. \end{aligned} \tag{64}$$

where for sake of brevity R_γ denotes $R(\gamma,\hat{\xi})$, and $\tilde{\omega}_\gamma$ indicates the skew-symmetric matrix associated to the proper pendulum velocity vector $\omega_m = [0\ 0\ \dot{\gamma}]^\top$.

Appendix C

For the computation of the dynamic equation the Lagrange equation for quasi-coordinates is applied. On this purpose, the computation of the kinetic and potential energy is required. On this purpose, the kinetic energy of the vertically-hinged pendulum is the following:

$$\mathcal{T} = \frac{1}{2}m_p[v_\xi^2 + (v_\eta + \omega_\zeta l_p)^2 + (v_\zeta - \omega_\eta l_p)^2] + \frac{1}{2}I_{xx}\omega_\xi^2 + \frac{1}{2}I_{yy}\omega_\eta^2 + \frac{1}{2}I_{zz}\omega_\zeta^2, \tag{65}$$

where its derivatives, with respect to the quasi-coordinates vector V_I and Ω_I is the following:

$$\begin{aligned}
\frac{\partial \mathcal{T}}{\partial v_\xi} &= m_p v_\xi \Longrightarrow \frac{d}{dt}\frac{\partial \mathcal{T}}{\partial v_\xi} = m_p \dot{v}_\xi,\\
\frac{\partial \mathcal{T}}{\partial v_\eta} &= m_p(v_\eta + \omega_\zeta l_p) \Longrightarrow \frac{d}{dt}\frac{\partial \mathcal{T}}{\partial v_\xi} = m_p(\dot{v}_\eta + \dot{\omega}_\zeta l_p),\\
\frac{\partial \mathcal{T}}{\partial v_\zeta} &= m_p(v_\zeta - \omega_\eta l_p) \Longrightarrow \frac{d}{dt}\frac{\partial \mathcal{T}}{\partial v_\xi} = m_p(\dot{v}_\zeta - \dot{\omega}_\eta l_p),\\
\frac{\partial \mathcal{T}}{\partial \omega_\xi} &= I_{xx}\omega_\xi \Longrightarrow \frac{d}{dt}\frac{\partial \mathcal{T}}{\partial \omega_\xi} = I_{xx}\dot{\omega}_\xi,\\
\frac{\partial \mathcal{T}}{\partial \omega_\eta} &= (I_{yy} + m_p l_p^2)\omega_\eta - m_p l_p v_\zeta \Longrightarrow \frac{d}{dt}\frac{\partial \mathcal{T}}{\partial \omega_\eta} = (I_{yy} + m_p l_p^2)\dot{\omega}_\eta - m_p l_p \dot{v}_\zeta,\\
\frac{\partial \mathcal{T}}{\partial \omega_\zeta} &= (I_{zz} + m_p l_p^2)\omega_\zeta + m_p l_p v_\eta \Longrightarrow \frac{d}{dt}\frac{\partial \mathcal{T}}{\partial \omega_\zeta} = (I_{zz} + m_p l_p^2)\dot{\omega}_\zeta + m_p l_p \dot{v}_\eta.
\end{aligned} \tag{66}$$

Such a derivatives are useful to solve the following Lagrange equations, explicitly defined for each DoF:

$$\begin{aligned}
&\frac{d}{dt}\frac{\partial \mathcal{T}}{\partial v_\xi} - \omega_\zeta \frac{\partial \mathcal{T}}{\partial v_\eta} + \omega_\eta \frac{\partial \mathcal{T}}{\partial v_\zeta} + G_{l_\xi} = F_{g_\xi},\\
&\frac{d}{dt}\frac{\partial \mathcal{T}}{\partial v_\eta} + \omega_\zeta \frac{\partial \mathcal{T}}{\partial v_\xi} - \omega_\xi \frac{\partial \mathcal{T}}{\partial v_\zeta} + G_{l_\eta} = F_{g_\eta},\\
&\frac{d}{dt}\frac{\partial \mathcal{T}}{\partial v_\zeta} - \omega_\eta \frac{\partial \mathcal{T}}{\partial v_\xi} + \omega_\xi \frac{\partial \mathcal{T}}{\partial v_\eta} + G_{l_\zeta} = F_{g_\zeta},\\
&\frac{d}{dt}\frac{\partial \mathcal{T}}{\partial \omega_\xi} - \omega_\zeta \frac{\partial \mathcal{T}}{\partial \omega_\eta} + \omega_\eta \frac{\partial \mathcal{T}}{\partial \omega_\zeta} - v_\zeta \frac{\partial \mathcal{T}}{\partial v_\eta} + v_\eta \frac{\partial \mathcal{T}}{\partial v_\zeta} + G_{r_\xi} = T_{g_\xi},\\
&\frac{d}{dt}\frac{\partial \mathcal{T}}{\partial \omega_\eta} + \omega_\zeta \frac{\partial \mathcal{T}}{\partial \omega_\xi} - \omega_\xi \frac{\partial \mathcal{T}}{\partial \omega_\zeta} + v_\zeta \frac{\partial \mathcal{T}}{\partial v_\xi} - v_\xi \frac{\partial \mathcal{T}}{\partial v_\zeta} + G_{r_\eta} = T_{g_\eta},\\
&\frac{d}{dt}\frac{\partial \mathcal{T}}{\partial \omega_\zeta} - \omega_\eta \frac{\partial \mathcal{T}}{\partial \omega_\xi} + \omega_\xi \frac{\partial \mathcal{T}}{\partial \omega_\eta} - v_\eta \frac{\partial \mathcal{T}}{\partial v_\xi} + v_\xi \frac{\partial \mathcal{T}}{\partial v_\eta} + G_{r_\zeta} = T_{g_\zeta}.
\end{aligned} \tag{67}$$

Finally, substituting Eq. (66) into (67), the following relations hold

$$\begin{aligned}
&m_p\dot{v}_\xi - m_p\omega_\zeta(v_\eta + \omega_\zeta l_p) + m_p\omega_\eta(v_\zeta - \omega_\eta l_p) + G_{l_\xi} = F_{g_\xi},\\
&m_p\dot{v}_\eta - m_p\omega_\zeta v_\xi - m_p\omega_\xi(v_\zeta - \omega_\eta l_p) + G_{l_\eta} = F_{g_\eta},\\
&m_p\dot{v}_\zeta - m_p\omega_\eta v_\xi - m_p\omega_\xi(v_\eta - \omega_\zeta l_p) + G_{l_\zeta} = F_{g_\zeta},\\
&I_\xi\dot{\omega}_{xi} + (I_{zz} - I_{yy})\omega_\eta\omega_\zeta + G_{r_\xi} = T_{g_\xi},\\
&(I_{yy} + m_p l_p^2)\dot{\omega}_\eta - m_p l_p \dot{v}_\zeta + (I_{zz} - I_{yy})\omega_\zeta\omega_\xi + m_p l_p v_\xi \omega_\eta\\
&+ m_p l_p \omega_\xi v_\eta + G_{r_\eta} = T_{g_\eta},\\
&(I_{zz} + m_p l_p^2)\dot{\omega}_\zeta + m_p l_p \dot{v}_\eta + (I_{yy} - I_{xx})\omega_\eta\omega_\xi\\
&- m_p l_p v_\zeta \omega_\xi + m_p l_p v_\xi \omega_\eta + G_{r_\zeta} = f_{pto},
\end{aligned} \tag{68}$$

where $G_{l_\xi}, t \mapsto G_{l_\xi}$, $G_{l_\eta}, t \mapsto G_{l_\eta}$, $G_{l_\zeta}, t \mapsto G_{l_\zeta}$, $G_{r_\xi}, t \mapsto G_{r_\xi}$, $G_{r_\eta}, t \mapsto G_{r_\eta}$ and $G_{r_\zeta}, t \mapsto G_{r_\zeta}$ are the effect of the gravity force acting on the system, mapped into the pendulum-fixed reference frame. In particular, the gravity effects are normally computed with respect to the inertial reference frame, going through the computation of the system potential energy:

$$\mathcal{U} = m_p g(z - l_p s_\delta c_\gamma + l_p c_\delta s_\theta s_\gamma - z_0 s_\delta + y_0 c_\delta s_\theta + z_0 c_\delta c_\theta). \tag{69}$$

Therefore, the resulting forces are

$$\begin{aligned}
G_{l_\zeta} &= \frac{\partial \mathcal{U}}{\partial z} = m_p g,\\
G_{r_\xi} &= \frac{\partial \mathcal{U}}{\partial \theta} = m_p g(l_p c_\delta c_\theta s_\gamma + y_0 c_\delta c_\theta - z_0 c_\delta s_\theta),\\
G_{r_\eta} &= \frac{\partial \mathcal{U}}{\partial \delta} = m_p g(-l_p c_\delta c_\gamma - l_p s_\delta s_\theta s_\gamma - x_0 c_\delta - y_0 s_\delta s_\theta - z_0 s_\delta c_\theta),\\
G_{r_\zeta} &= \frac{\partial \mathcal{U}}{\partial \epsilon} = m_p g(l_p s_\delta s_\gamma + l_p c_\delta s_\theta c_\gamma).
\end{aligned} \tag{70}$$

Alternatively, the dynamic equation can be directly computed in linear form, applying the following expression

$$\frac{d}{dt}\frac{\partial \mathcal{T}}{\partial \dot{p}} - \frac{\partial \mathcal{T}}{\partial p} + \frac{\partial \mathcal{U}}{\partial p} = F_{rc}. \tag{71}$$

For such a case, the velocity of the pendulum is defined in linear force, neglecting all the nonlinear effects, hence looking as follows:

$$\begin{aligned}
v_{EF_\xi} &= \dot{x} + z_0\dot{\delta} - y_0\dot{\psi},\\
v_{EF_\eta} &= \dot{y} - z_0\dot{\theta} + x_0\dot{\psi} + l_p(\dot{\psi} + \dot{\gamma}),\\
v_{EF_\zeta} &= \dot{z} + y_0\dot{\theta} - x_0\dot{\delta} - l_p\dot{\delta},\\
\omega_{EF_\xi} &= \dot{\theta},\\
\omega_{EF_\eta} &= \dot{\delta},\\
\omega_{EF_\zeta} &= \dot{\psi} + \dot{\gamma}.
\end{aligned} \tag{72}$$

Finally, each term of the Lagrangian of Eq. (71) is explicit ally computed, and expressed as follows

$$\begin{aligned}
&\frac{\partial \mathcal{T}}{\partial \dot{x}} = m_p(\dot{x} + z_0\dot{\delta} - y_0\dot{\psi})\\
&\Longrightarrow \frac{d}{dt}\frac{\partial \mathcal{T}}{\partial \dot{x}} = m_p(\ddot{x} + z_0\ddot{\delta} - y_0\ddot{\psi}),\\
&\frac{\partial \mathcal{T}}{\partial \dot{y}} = m_p(\dot{y} - z_0\dot{\theta} + x_0\dot{\psi} + l_p(\dot{\psi} + \dot{\epsilon}))\\
&\Longrightarrow \frac{d}{dt}\frac{\partial \mathcal{T}}{\partial \dot{y}} = m_p(\ddot{y} - z_0\ddot{\theta} + x_0\ddot{\psi} + l_p(\ddot{\psi} + \ddot{\gamma})),\\
&\frac{\partial \mathcal{T}}{\partial \dot{z}} = m_p(\dot{z} + y_0\dot{\theta} - x_0\dot{\delta} - l_p\dot{\delta})\\
&\Longrightarrow \frac{d}{dt}\frac{\partial \mathcal{T}}{\partial \dot{z}} = m_p(\ddot{z} + y_0\ddot{\theta} - x_0\ddot{\delta} - l_p\ddot{\delta}),\\
&\frac{\partial \mathcal{T}}{\partial \dot{\theta}} = I_{xx}\dot{\theta} + m_p y_0(\dot{z} + y_0\dot{\theta} - x_0\dot{\delta} - l_p\dot{\delta}) - m_p z_0(\dot{y} - z_0\dot{\theta} + x_0\dot{\psi} + l_p\dot{\psi})\\
&\Longrightarrow \frac{d}{dt}\frac{\partial \mathcal{T}}{\partial \dot{\theta}} = I_{xx}\ddot{\theta} + m_p y_0(\ddot{z} + y_0\ddot{\theta} - x_0\ddot{\delta} - l_p\ddot{\delta})\\
&\qquad - m_p z_0(\ddot{y} - z_0\ddot{\theta} + x_0\ddot{\psi} + l_p\ddot{\psi}),\\
&\frac{\partial \mathcal{T}}{\partial \dot{\delta}} = I_{yy}\dot{\delta} + m_p z_0(\dot{x} + z_0\dot{\delta} - y_0\dot{\psi}) - m_p(x_0 + l_p)(\dot{z} + y_0\dot{\theta} - x_0\dot{\delta} - l_p\dot{\delta})\\
&\Longrightarrow \frac{d}{dt}\frac{\partial \mathcal{T}}{\partial \dot{\delta}} = I_{yy}\ddot{\delta} + m_p z_0(\ddot{x} + z_0\ddot{\delta} - y_0\ddot{\psi})\\
&\qquad - m_p(x_0 + l_p)(\ddot{z} + y_0\ddot{\theta} - x_0\ddot{\delta} - l_p\ddot{\delta}),\\
&\frac{\partial \mathcal{T}}{\partial \dot{\psi}} = -m_p y_0(\dot{x} + z_0\dot{\delta} - y_0\dot{\psi}) + (x_0 + l_p)m_p(\dot{y} - z_0\dot{\theta} + (x_0 + l_p)\dot{\psi} + l_p\dot{\gamma})\\
&\quad + I_{zz}(\dot{\psi} + \dot{\gamma})\\
&\Longrightarrow \frac{d}{dt}\frac{\partial \mathcal{T}}{\partial \dot{\psi}} = -m_p y_0(\ddot{x} + z_0\ddot{\delta} - y_0\ddot{\psi})\\
&\qquad + (x_0 + l_p)m_p(\ddot{y} - z_0\ddot{\theta} + (x_0 + l_p)\ddot{\psi} + l_p\ddot{\gamma}) + I_{zz}(\ddot{\psi} + \ddot{\gamma}),\\
&\frac{\partial \mathcal{T}}{\partial \dot{\gamma}} = m_p l_p(\dot{y} - z_0\dot{\theta} + x_0\dot{\psi} + l_p(\dot{\psi} + \dot{\gamma}) + I_{zz}(\dot{\psi} + \dot{\gamma}))\\
&\Longrightarrow \frac{d}{dt}\frac{\partial \mathcal{T}}{\partial \dot{\gamma}} = m_p l_p(\ddot{y} - z_0\ddot{\theta} + x_0\ddot{\psi} + l_p(\ddot{\psi} + \ddot{\gamma}) + I_{zz}(\ddot{\psi} + \ddot{\gamma})).
\end{aligned} \tag{73}$$

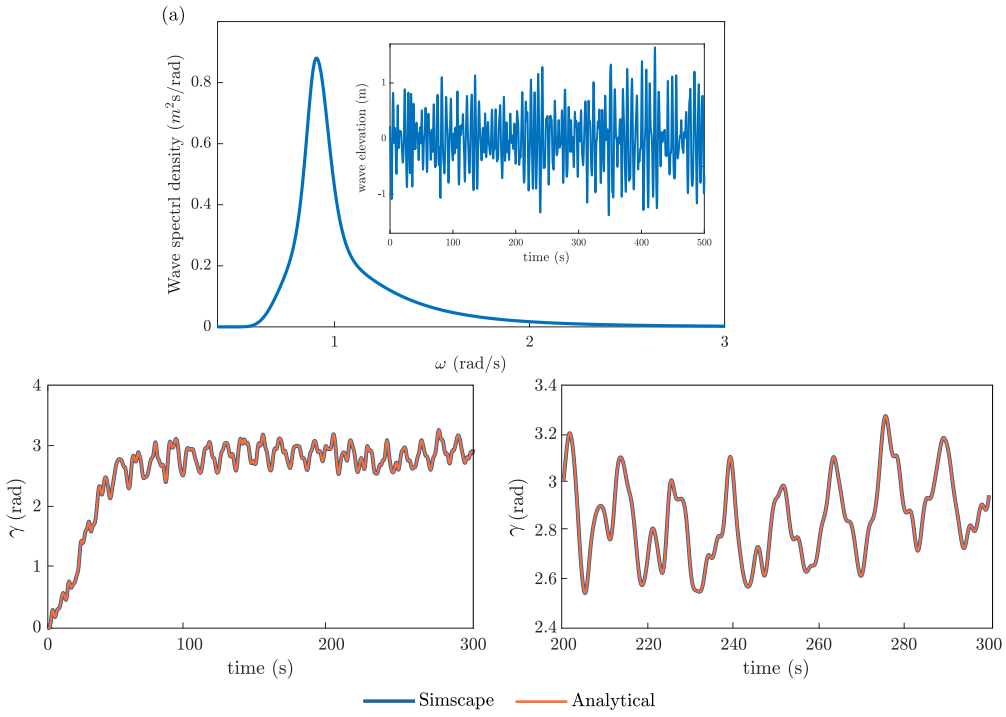

Fig. 10. Pendulum rotation angle simulating the floater motion generated by an irregular wave signal: (a) Jonswap Spectrum representation and time series of an irregular wave characterized by $T_e = 6.2$ s and $H_s = 2$ m, (b) Comparison between the analytical model and the Simscape model, simulating an irregular wave signal, (c) Zoom in on the generated pendulum motion.

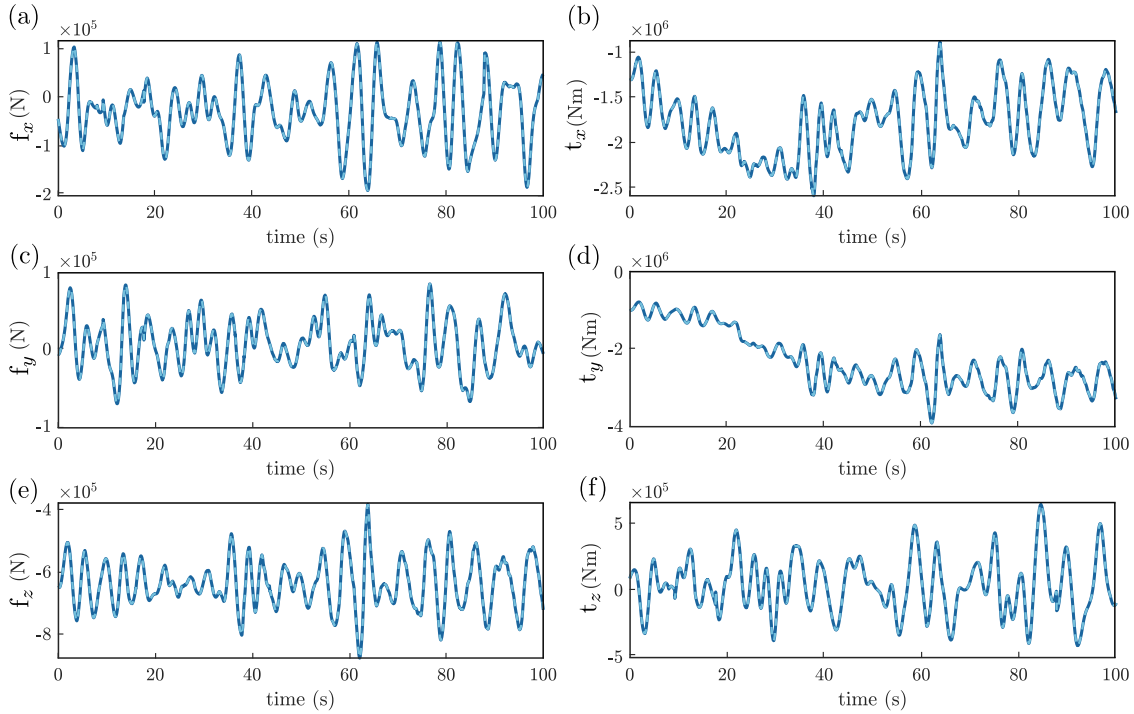

Fig. 11. Reaction forces acting on the floater through the pendulum constraints: comparison between the analytical model and the Simscape model, simulating an irregular wave signal. The panel figure shows (a) the reaction force acting on the x-axis, (b) the reaction torque acting on the x-axis, (c) the reaction force acting on the y-axis, (d) the reaction torque acting on the y-axis, (e) the reaction force acting on the z-axis, and (f) the reaction torque acting on the z-axis.

Appendix D

Figs. 10 and 11 compare the time series of the reaction forces F_{rc} and pendulum rotation angle γ, as obtained from both the analytical and Simscape models. In this case, the pre-defined signal vector q is generated by an irregular wave, obtained through the simulation of a JONSWAP spectrum [67] characterized by $T_e = 6.2$ s and $H_s = 2$ m.

References

[1] Wang F, Harindintwali JD, Yuan Z, Wang M, Wang F, Li S, et al. Technologies and perspectives for achieving carbon neutrality. Innovation 2021;2(4):100180. http://dx.doi.org/10.1016/j.xinn.2021.100180.

[2] Gunn K, Stock-Williams C. Quantifying the global wave power resource. Renew Energy 2012;44:296–304. http://dx.doi.org/10.1016/j.renene.2012.01.101.

[3] Terrero González A, Dunning P, Howard I, McKee K, Wiercigroch M. Is wave energy untapped potential? Int J Mech Sci 2021;205:106544. http://dx.doi.org/10.1016/j.ijmecsci.2021.106544.

[4] Trueworthy A, DuPont B. The wave energy converter design process: Methods applied in industry and shortcomings of current practices. J Mar Sci Eng 2020;8(11):932. http://dx.doi.org/10.3390/jmse8110932.

[5] Giglio E, Petracca E, Paduano B, Moscoloni C, Giorgi G, Sirigu SA. Estimating the cost of wave energy converters at an early design stage: A bottom-up approach. Sustainability 2023;15(8):6756. http://dx.doi.org/10.3390/su15086756.

[6] Cummins WE. The impulse response function and ship motions. In: Symposium on ship theory at the institut flir schiffbau der universitit hamburg. Hamburg; 1962.

[7] Babarit A, Delhommeau G. Theoretical and numerical aspects of the open source BEM solver NEMOH. In: 11th European wave and tidal energy conference, nantes, France. 2015.

[8] Yu Y-H, Lawson MJ, Kelley Ruehl, Carlos A Michelén Ströfer. Development and demonstration of the WEC-sim wave energy converter simulation tool. In: 2nd marine energy technology symposium. Seattle, WA; 2014.

[9] Penalba M, Ringwood JV. A high-fidelity wave-to-wire model for wave energy converters. Renew Energy 2019;134:367–78. http://dx.doi.org/10.1016/j.renene.2018.11.040.

[10] Faedo N, Carapellese F, Pasta E, Mattiazzo G. On the principle of impedance-matching for underactuated wave energy harvesting systems. Appl Ocean Res 2022;118. http://dx.doi.org/10.1016/j.apor.2021.102958.

[11] Wang T. Pendulum-based vibration energy harvesting: Mechanisms, transducer integration, and applications. Energy Convers Manage 2023;276:116469. http://dx.doi.org/10.1016/j.enconman.2022.116469.

[12] Giorgi G, Carapellese F, Mattiazzo G. Stepping-up wave energy extraction in all degrees of freedom by combining pendulum and gyroscopic effects. In: IFToMM Italy 2022. Mechanisms and Machine Science. 2022, p. 882–90. http://dx.doi.org/10.1007/978-3-031-10776-4_101.

[13] Ma Y, Ai S, Yang L, Zhang A, Liu S, Zhou B. Hydrodynamic performance of a pitching float wave energy converter. Energies 2020;13(7):1801. http://dx.doi.org/10.3390/en13071801.

[14] Josset C, Babarit A, Clément AH. A wave-to-wire model of the SEAREV wave energy converter. Proc Inst Mech Eng M 2007;221(2):81–93. http://dx.doi.org/10.1243/14750902JEME48.

[15] Clement A, Babarit A, Gilloteaux J-C. The searev wave energy converter. In: European wave and tidal energy conference. Glasgow, United Kingdom; 2005.

[16] Cordonnier J, Gorintin F, De Cagny A, Clément A, Babarit A. SEAREV: Case study of the development of a wave energy converter. Renew Energy 2015;80:40–52. http://dx.doi.org/10.1016/j.renene.2015.01.061.

[17] Durand M, Babarit A, Petinotti B, Clement A. Experimental validation of the performances of the SEAREV wave energy converter with real-time latching control. In: 7th European wave and tidal energy conference. Porto, Portugal; 2007.

[18] AMOG. AMOG Wave Energy Converter. URL https://amog.consulting/products/wave-energy-converter.

[19] Serena A, Molinas M, Cobo I. Design of a direct drive wave energy conversion system for the seaquest concept. Energy Procedia 2012;20:271–80. http://dx.doi.org/10.1016/j.egypro.2012.03.027.

[20] Wu J, Qian C, Zheng S, Chen N, Xia D, Göteman M. Investigation on the wave energy converter that reacts against an internal inverted pendulum. Energy 2022;247:123493. http://dx.doi.org/10.1016/j.energy.2022.123493.

[21] Yerrapragada K, Ansari MH, Karami MA. Enhancing power generation of floating wave power generators by utilization of nonlinear roll-pitch coupling. Smart Mater Struct 2017;26(9):094003. http://dx.doi.org/10.1088/1361-665X/aa7710.

[22] Wello O. The Wello Penguin Wave Energy Converter. URL https://wello.eu/the-penguin-2/.

[23] Boren BC, Lomonaco P, Batten BA, Paasch RK. Design, development, and testing of a scaled vertical axis pendulum wave energy converter. IEEE Trans Sustain Energy 2017;8(1):155–63. http://dx.doi.org/10.1109/TSTE.2016.2589221.

[24] Wang T, Wang H. Multistable pendulum wave energy harvesting under multidirectional irregular excitations. IEEE/ASME Trans Mechatronics 2024;1–9. http://dx.doi.org/10.1109/TMECH.2024.3400989.

[25] Crowley S, Porter R, Taunton D, Wilson P. Modelling of the WITT wave energy converter. Renew Energy 2018;115:159–74. http://dx.doi.org/10.1016/j.renene.2017.08.004.

[26] Kanki H, Arii S, Furusawa T, Otoyo T. Development of advanced wave power generation system by applying gyroscopic moment.

[27] Townsend NC, Shenoi RA. Modelling and analysis of a single gimbal gyroscopic energy harvester. Nonlinear Dynam 2013;72(1–2):285–300. http://dx.doi.org/10.1007/s11071-012-0713-7.

[28] Bracco G, Giorcelli E, Mattiazzo G. ISWEC: A gyroscopic mechanism for wave power exploitation. Mech Mach Theory 2011;46(10):1411–24. http://dx.doi.org/10.1016/j.mechmachtheory.2011.05.012.

[29] Salcedo F, Ruiz-Minguela P, Rodriguez Arias R, Ricci P, Santos-Mujica M. Oceantec: Sea trials of a quarter scale prototype. In: Proceedings of 8th European wave tidal energy conference. 2009.

[30] Pei Z, Jing H, Tang Z. Modeling and test results of an innovative gyroscope wave energy converter. Appl Sci 2021;11(10):4359. http://dx.doi.org/10.3390/app11104359.

[31] Clemente D, Rosa-Santos P, Taveira-Pinto F, Martins P. Influence of platform design and power take-off characteristics on the performance of the E-motions wave energy converter. Energy Convers Manage 2021;244:114481. http://dx.doi.org/10.1016/j.enconman.2021.114481.

[32] McCabe A, Bradshaw A, Meadowcroft J, Aggidis G. Developments in the design of the PS Frog Mk 5 wave energy converter. Renew Energy 2006;31(2):141–51. http://dx.doi.org/10.1016/j.renene.2005.08.013.

[33] Chen Z, Zhou B, Zhang L, Li C, Zang J, Zheng X, et al. Experimental and numerical study on a novel dual-resonance wave energy converter with a built-in power take-off system. Energy 2018;165:1008–20. http://dx.doi.org/10.1016/j.energy.2018.09.094.

[34] Aggidis G, Taylor C. Overview of wave energy converter devices and the development of a new multi-axis laboratory prototype. IFAC-PapersOnLine 2017;50(1):15651–6. http://dx.doi.org/10.1016/j.ifacol.2017.08.2391.

[35] Guo B, Ringwood JV. Non-linear modeling of a vibro-impact wave energy converter. IEEE Trans Sustain Energy 2021;12(1):492–500. http://dx.doi.org/10.1109/TSTE.2020.3007926.

[36] Giorgi G, Faedo N. Performance enhancement of a vibration energy harvester via harmonic time-varying damping: A pseudospectral-based approach. Mech Syst Signal Process 2022;165:108331. http://dx.doi.org/10.1016/j.ymssp.2021.108331.

[37] Carapellese F, Pasta E, Faedo N, Giorgi G. Dynamic analysis and performance assessment of the inertial sea wave energy converter (ISWEC) device via harmonic balance. In: 14th IFAC conference on control applications in marine systems, robotics and vehicles. Lyngby, Denmark; 2022, http://dx.doi.org/10.1016/j.ifacol.2022.10.467.

[38] Bonfanti M, Faedo N, Mattiazzo G. Towards efficient control synthesis for nonlinear wave energy conversion systems: Impedance-matching meets the spectral-domain. Nonlinear Dynam 2024;112(13):11085–109. http://dx.doi.org/10.1007/s11071-024-09600-0.

[39] Carapellese F, Paduano B, Pasta E, Papini G, Faedo N, Mattiazzo G. Nonlinear dynamic analysis and control synthesis for the swinging omnidirectional (SWINGO) wave energy converter. IFAC-PapersOnLine 2023;56(2):11723–8. http://dx.doi.org/10.1016/j.ifacol.2023.10.540.

[40] Sirigu SA, Vissio G, Bracco G, Giorcelli E, Passione B, Raffero M, et al. ISWEC design tool. Int J Mar Energy 2016;15:201–13. http://dx.doi.org/10.1016/j.ijome.2016.04.011.

[41] Merigaud A, Ringwood JV. A nonlinear frequency-domain approach for numerical simulation of wave energy converters. IEEE Trans Sustain Energy 2018;9(1):86–94. http://dx.doi.org/10.1109/TSTE.2017.2716826.

[42] Sirigu SA, Foglietta L, Giorgi G, Bonfanti M, Cervelli G, Bracco G, et al. Techno-economic optimisation for a wave energy converter via genetic algorithm. J Mar Sci Eng 2020;8:482. http://dx.doi.org/10.3390/jmse8070482.

[43] Faedo N, Dores Piuma FJ, Giorgi G, Ringwood JV. Nonlinear model reduction for wave energy systems: A moment-matching-based approach. Nonlinear Dynam 2020;102(3):1215–37. http://dx.doi.org/10.1007/s11071-020-06028-0.

[44] Faedo N, Pasta E, Carapellese F, Orlando V, Pizzirusso D, Basile D, et al. Energy-maximising experimental control synthesis via impedance-matching for a multi degree-of-freedom wave energy converter. In: 14th IFAC conference on control applications in marine systems, robotics and vehicles. Lyngby, Denmark; 2022.

[45] Carapellese F, Pasta E, Paduano B, Faedo N, Mattiazzo G. Intuitive LTI energy-maximising control for multi-degree of freedom wave energy converters: The PeWEC case. Ocean Eng 2022;256:111444. http://dx.doi.org/10.1016/j.oceaneng.2022.111444.

[46] Pei L, Chong AS, Pavlovskaia E, Wiercigroch M. Computation of periodic orbits for piecewise linear oscillator by harmonic balance methods. Commun Nonlinear Sci Numer Simul 2022;108:106220. http://dx.doi.org/10.1016/j.cnsns.2021.106220.

[47] Xu X, Wiercigroch M, Cartmell M. Rotating orbits of a parametrically-excited pendulum. Chaos Solitons Fractals 2005;23(5):1537–48. http://dx.doi.org/10.1016/j.chaos.2004.06.053.

[48] Najdecka A, Narayanan S, Wiercigroch M. Rotary motion of the parametric and planar pendulum under stochastic wave excitation. Int J Non-Linear Mech 2015;71:30–8. http://dx.doi.org/10.1016/j.ijnonlinmec.2014.12.008.

[49] Pasta E, Faedo N, Mattiazzo G, Ringwood JV. Towards data-driven and data-based control of wave energy systems: Classification, overview, and critical assessment. Renew Sustain Energy Rev 2023;188:113877. http://dx.doi.org/10.1016/j.rser.2023.113877.

[50] Vissio G, Valério D, Bracco G, Beirão P, Pozzi N, Mattiazzo G. ISWEC linear quadratic regulator oscillating control. Renew Energy 2017;103:372–82. http://dx.doi.org/10.1016/j.renene.2016.11.046.

[51] Bracco G, Cagninei A, Giorcelli E, Mattiazzo G, Poggi D, Raffero M. Experimental validation of the ISWEC wave to PTO model. Ocean Eng 2016;120. http://dx.doi.org/10.1016/j.oceaneng.2016.05.006.
[52] Pozzi N, Bracco G, Passione B, Sirigu SA, Mattiazzo G. PeWEC: Experimental validation of wave to PTO numerical model. Ocean Eng 2018;167:114–29. http://dx.doi.org/10.1016/j.oceaneng.2018.08.028.
[53] Clemente D, Rosa-Santos P, Taveira-Pinto F, Martins P, Paulo-Moreira A. Proof-of-concept study on a wave energy converter based on the roll oscillations of multipurpose offshore floating platforms. Energy Convers Manage 2020;224:113363. http://dx.doi.org/10.1016/j.enconman.2020.113363.
[54] Pei Z, Jing H, Tang Z, Fu Y. Experimental validation of a gyroscope wave energy converter for autonomous underwater vehicles. Appl Sci 2021;11(23):11115. http://dx.doi.org/10.3390/app112311115.
[55] Yang Y, Reyes R, Gonzalez C, Echevarria S. Development of an angularly oscillating wave energy converter. In: Volume 4: Energy systems analysis, thermodynamics and sustainability; combustion science and engineering; nanoengineering for energy, parts a and b. ASMEDC; 2011, p. 1135–42. http://dx.doi.org/10.1115/IMECE2011-62359.
[56] Guo B, Wang T, Jin S, Duan S, Yang K, Zhao Y. A review of point absorber wave energy converters. J Mar Sci Eng 2022;10(10):1534. http://dx.doi.org/10.3390/jmse10101534, URL https://www.mdpi.com/2077-1312/10/10/1534.
[57] Windt C, Davidson J, Ringwood JV. High-fidelity numerical modelling of ocean wave energy systems: A review of computational fluid dynamics-based numerical wave tanks. Renew Sustain Energy Rev 2018;93:610–30. http://dx.doi.org/10.1016/j.rser.2018.05.020.
[58] Giorgi G. The onset of instability in a parametric resonance energy harvester under panchromatic excitations. Int J Mech Sci 2024;281:109544. http://dx.doi.org/10.1016/j.ijmecsci.2024.109544.
[59] Giorgi G. Embedding parametric resonance in a 2:1 wave energy converter to get a broader bandwidth. Renew Energy 2024;222:119928. http://dx.doi.org/10.1016/j.renene.2023.119928.
[60] Falnes J. Ocean waves and oscillating systems. Cambridge University Press; 2002, http://dx.doi.org/10.1017/CBO9780511754630.
[61] Faedo N, Bussi U, Peña-Sanchez Y, Windt C, Ringwood JV. A simple and effective excitation force estimator for wave energy systems. IEEE PES Trans Sustain Energy 2021.
[62] Duarte T, Gueydon S, Jonkman J, Sarmento A. Computation of wave loads under multidirectional sea states for floating offshore wind turbines. In: Volume 9B: Ocean renewable energy. American Society of Mechanical Engineers; 2014, http://dx.doi.org/10.1115/OMAE2014-24148.
[63] Faedo N, Peña-Sanchez Y, Ringwood JV. Finite-order hydrodynamic model determination for wave energy applications using moment-matching. Ocean Eng 2018;163:251–63. http://dx.doi.org/10.1016/j.oceaneng.2018.05.037.
[64] Faedo N, Peña-Sanchez Y, Carapellese F, Mattiazzo G, Ringwood JV. LMI-based passivisation of LTI systems with application to marine structures. 2021, http://dx.doi.org/10.1109/TSTE.2021.3108576.
[65] Ahamed R, McKee K, Howard I. Advancements of wave energy converters based on power take off (PTO) systems: A review. Ocean Eng 2020;204:107248. http://dx.doi.org/10.1016/j.oceaneng.2020.107248.
[66] Hasan Maheen M, Yang Y. Wave energy converters with rigid hull encapsulation: A review. Sustain Energy Technol Assess 2023;57:103273. http://dx.doi.org/10.1016/j.seta.2023.103273.
[67] Merigaud A, Ringwood JV. Free-surface time-series generation for wave energy applications. IEEE J Ocean Eng 2018;43:19–35. http://dx.doi.org/10.1109/JOE.2017.2691199.
[68] Merigaud A, Ringwood JV. Incorporating ocean wave spectrum information in short-term free-surface elevation forecasting. IEEE J Ocean Eng 2019;44(2):401–14. http://dx.doi.org/10.1109/JOE.2018.2822498.
[69] Han N, Lu P, Li Z. An approximate technique to test chaotic region in a rotating pendulum system with bistable characteristics. Nonlinear Dynam 2021;104(1):191–214. http://dx.doi.org/10.1007/s11071-021-06274-w.
[70] Cai Q, Zhu S. Nonlinear double-mass pendulum for vibration-based energy harvesting. Nonlinear Dynam 2024;112(7):5109–28. http://dx.doi.org/10.1007/s11071-023-09236-6.
[71] Graves J, Zhu M. Design and experimental validation of a pendulum energy harvester with string-driven single clutch mechanical motion rectifier. Sensors Actuators A 2022;333:113237. http://dx.doi.org/10.1016/j.sna.2021.113237.
[72] Zhang X, Zhang H, Zhou X, Sun Z. Recent advances in wave energy converters based on nonlinear stiffness mechanisms. Appl Math Mech 2022;43(7):1081–108. http://dx.doi.org/10.1007/s10483-022-2864-6.
[73] Zhang H, Zhou X, Xu D, Zou W, Ding J, Xia S. Nonlinear stiffness mechanism for high-efficiency and broadband raft-type wave energy converters. Mech Syst Signal Process 2022;177:109168. http://dx.doi.org/10.1016/j.ymssp.2022.109168.
[74] Dotti FE, Virla JN. Nonlinear dynamics of the parametric pendulum with a view on wave energy harvesting applications. J Comput Nonlinear Dyn 2021;16(6). http://dx.doi.org/10.1115/1.4050699, URL https://asmedigitalcollection.asme.org/computationalnonlinear/article/16/6/061007/1106107/Nonlinear-Dynamics-of-the-Parametric-Pendulum-With.
[75] Zhou X, Zhang H, Jin H, Liu C, Xu D. Numerical and experimental investigation of a hinged wave energy converter with negative stiffness mechanism. Int J Mech Sci 2023;245:108103. http://dx.doi.org/10.1016/j.ijmecsci.2023.108103.
[76] Zhang H, Zhang J, Zhou X, Shi Q, Xu D, Sun Z, et al. Robust performance improvement of a raft-type wave energy converter using a nonlinear stiffness mechanism. Int J Mech Sci 2021;211:106776. http://dx.doi.org/10.1016/j.ijmecsci.2021.106776.
[77] Ringwood JV, Bacelli G, Fusco F. Energy-maximizing control of wave-energy converters: The development of control system technology to optimize their operation. IEEE Control Syst 2014;34:30–55. http://dx.doi.org/10.1109/MCS.2014.2333253.
[78] Faedo N. Optimal control and model reduction for wave energy systems: A moment-based approach. National University of Ireland Maynooth; 2020.
[79] Said HA, Ringwood JV. Grid integration aspects of wave energy—Overview and perspectives. IET Renew Power Gener 2021;15(14):3045–64. http://dx.doi.org/10.1049/rpg2.12179.
[80] Meirovitch L. Hybrid state equations of motion for flexible bodies in terms of quasi-coordinates. J Guid Control Dyn 1991;14(5):1008–13. http://dx.doi.org/10.2514/3.20743.
[81] Carapellese F, Pasta E, Sirigu SA, Faedo N. SWINGO: Conceptualisation, modelling, and control of a swinging omnidirectional wave energy converter. Mech Syst Signal Process 2023.
[82] Paduano B, Carapellese F, Pasta E, Bonfanti M, Sirigu SA, Basile D, et al. Experimental and numerical investigation on the performance of a Moored pitching wave energy conversion system. IEEE J Ocean Eng 2024;49(3):802–20. http://dx.doi.org/10.1109/JOE.2024.3353372.
[83] Bonfanti M, Sirigu SA, Giorgi G, Dafnakis P, Bracco G, Mattiazzo G. A passive control strategy applied to the iswec device: Numerical modelling and experimental tests. Int J Mech Control 2020.
[84] Mattiazzo G. State of the art and perspectives of wave energy in the Mediterranean sea: Backstage of ISWEC. Front Energy Res 2019;7. http://dx.doi.org/10.3389/fenrg.2019.00114.
[85] Alexander R. Diagonally implicit Runge–Kutta methods for stiff O.D.E.'s. SIAM J Numer Anal 1977;14(6):1006–21. http://dx.doi.org/10.1137/0714068.
[86] Fusco F, Ringwood JV. A simple and effective real-time controller for wave energy converters. IEEE Trans Sustain Energy 2013;4(1):21–30. http://dx.doi.org/10.1109/TSTE.2012.2196717.